Politecnico di Torino

DENERG Department of Energy "Galileo Ferraris"

Master's Degree Course in Electrical Engineering

Master's Thesis

in

Design and multiphysics analysis of a 3D printed winding with fluid cooling channels in a multi-three-phase motor

Student:
Matteo Coccollone

Supervisor:
Prof. Paolo Gugliemi

Co-Supervisor:
Prof. Flaviana Calignano

Academic Year 2023/2024

Abstract

The work focuses on the design and multiphysics analysis of a 3D-printed winding with fluid cooling channels for a multi-three-phase surface permanent magnet motor. The main objective is to reduce the motor's supply voltage from 400 V to 20 V while maintaining a power output of 20 kW. To manage the increase in Joule losses, an internal cooling solution was developed within the windings, with channels designed for the passage of a coolant fluid. The winding was manufactured using powder bed fusion (PBF-LB/M) technology with AlSi10Mg material. The multiphysics simulations, conducted through *Finite Element Analysis* (FEA) using COMSOL software, were compared with measurements taken from a printed prototype. This work demonstrates how 3D printing and FEA simulations can optimize the design and thermal efficiency of electrical windings.

Contents

List of Figures

List of Tables

Introduction

The electric motor industry has evolved considerably in recent decades, particularly in terms of energy efficiency, reliability, and emission reduction. However, one of the biggest challenges remains thermal management, especially in applications requiring high power densities and compact components. The dissipation of heat from power losses in the windings is essential to prevent overheating and improve motor performance.

With the advent of additive manufacturing, better known as 3D printing, it is now possible to overcome some limitations of traditional production methods. In particular, the ability to create complex geometries with internal cooling channels represents a significant innovation in electric motor design. 3D printing allows optimization of the windings' structure in terms of size, shape, and thermal efficiency.

This work aims to design and analyze a winding for a multi-three-phase surface permanent magnet motor, made using additive manufacturing and equipped with internal fluid cooling channels. By reducing the supply voltage from 400 V to 20 V while maintaining a power output of 20 kW, a significant thermal challenge arises due to increased Joule losses. The solution involves direct fluid cooling of the windings, specifically using a water-glycol mixture.

The design was developed in phases: from the choice of material (AlSi10Mg) to the creation of the winding using PBF-LB/M technology, followed by validation through multiphysics simulations using COMSOL. These simulations were compared with experimental data obtained from a physical prototype to assess the effectiveness of the proposed solutions.

The thesis is structured as follows: Chapter 1 provides an overview of additive manufacturing technologies, focusing on the PBF-LB/M technique used for the winding. Chapter 2 describes the design of the entire winding, including the optimization of the cooling channels. Chapter 3 reports the printing results of the first winding version, while Chapter 4 covers the winding revision. Chapter 5 focuses on the multiphysics analysis with COMSOL, and Chapter 6 contains prototype measurements and performance evaluation. Finally, general conclusions and future applications are discussed.

Chapter 1

Additive manufacturing of metallic materials

In product development, the technology with which prototypes can be produced directly from digital data is called *Additive Manufacturing* (AM). This technology makes it possible to develop a product from a three-dimensional *Computer Aided Design* (3D CAD) file without the need for a process plan. The ASTM Committee F42 on Additive Manufacturing Technologies, founded in 2009, has been working on standardizing the terminology for AM. According to the first standard, ASTM F2792-10, AM is defined as "The process of joining materials to make objects from 3D model data, usually layer upon layer, as opposed to subtractive manufacturing technologies." There are multiple terms in the literature and common language to describe AM, the most commonly used synonyms being: additive fabrication, additive layer manufacturing, direct digital manufacturing, 3D printing and freeform fabrication [5]. Compared to most other manufacturing technologies, AM has relatively few manufacturing constraints, which allows for an optimization-oriented design process. To understand which products or components are more advantageous to produce using AM than conventional methods, four key points can be listed:

- design focus on reducing the number of parts in the system;
- the ability to customize products or components;
- the fact that this production method allows for lighter constructions than conventional methods;

- the ability to create more efficient designs, as a more complex part does not incur higher production costs than a simple part [12].

1.1 Overview of the various AM technologies for metals

Many technologies are grouped under the term additive manufacturing, the general function of which is to produce a product, starting from a 3D model, as layer upon layer of material is added. It is possible to classify various AM technologies according to various parameters, such as: types of materials used, material solidification process, and deposition ways. Based on ASTM F42 committee guidelines, seven main processes can be classified:

1. *binder jetting* (BJT), additive manufacturing process in which a liquid bonding agent is selectively deposited to join powder materials;
2. *directed energy deposition* (DED), additive manufacturing process in which focused thermal energy is used to fuse materials by melting as they are being deposited;
3. *material extrusion* (MEX), additive manufacturing process in which material is selectively dispensed through a nozzle or orifice;
4. *material jetting* (MJT), additive manufacturing process in which droplets of feedstock material are selectively deposited;
5. *powder bed fusion* (PBF), additive manufacturing process in which thermal energy selectively fuses regions of a powder bed;
6. *sheet lamination* (SHL), additive manufacturing process in which sheets of material are bonded to form a part;
7. *vat photopolymerization* (VPP), additive manufacturing process in which liquid photopolymer in a vat is selectively cured by light-activated polymerization [13].

In the remainder of this thesis, the power bed fusion category will be examined, with a particular focus on *Powder Bed Fusion using a Laser Beam in a Metallic material* (PBF-LB/M)[1], as this method will be employed for

[1]ISO/ASTM 52900:2021(E)

prototyping the component that is the subject of this study. It is important to note that this technology was previously known as *Direct Metal Laser Sintering* (DMLS) or *Selective Laser Melting* (SLM).

1.2 PBF-LB/M

PBF-LB/M was developed to produce metal parts from a metal powder. Specifically, it is a power-bed fusion process in which a high-intensity laser is used to melt one layer of metal powder after another, according to the specifications in the CAD of the component. This process requires several steps, as can be seen in the figure 1.1. First, modeling is done in CAD software, then the STL (*Standard Tessellation Language*) file is loaded into the PBF-LB/M machine, and this file must be processed by software to process the appropriate support structures for each overhanging feature and generate slice data for laser scanning of each layer. The build process starts with laying the metal powder state on a support plate in the build chamber. Once the powder has been applied, a high-energy laser is used to fuse the selected areas according to the processed CAD file. Once this melting process is complete, the build platform is lowered and another layer of metal powder is applied, after which the laser is used again to form a new layer by melting the new powder. This process is repeated until the component is finished. Due to the high temperatures required to melt the metal powder, the component is produced in a controlled oxygen atmosphere. To prevent oxidation and reduce the risk of fires that can occur with reactive materials, an inert gas such as argon or nitrogen is used. [14].

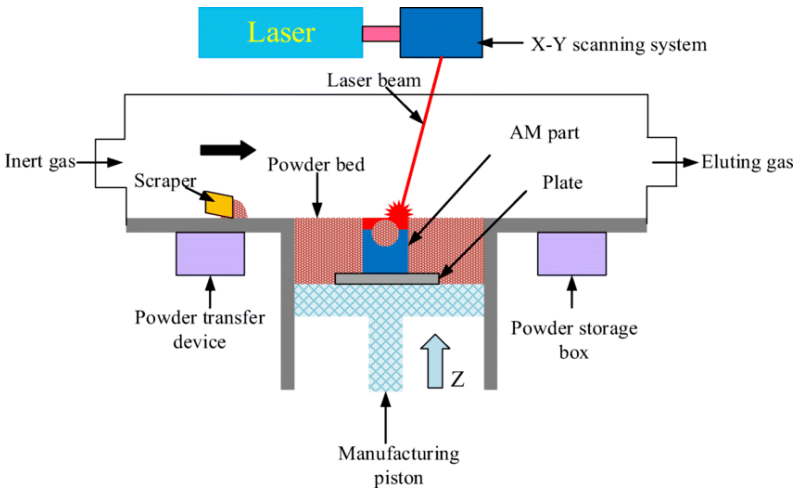

Figure 1.1: PBF-LB/M process [2].

[2]Source: researchgate.net

Since the components are built layer by layer, it is possible to design internal features and passages that would be unachievable through traditional casting or machining methods. Complex geometries and assemblies with multiple components can be simplified into fewer parts, making assembly more cost-effective. PBF-LB/M is used to produce lightweight, cellular-like structures. Inspired by natural systems, these cellular metal structures are used in various industrial applications such as heat exchangers, the automotive industry, and aerospace, thanks to their valuable characteristics including low density, high strength, good energy absorption, and excellent thermal properties [5].

1.2.1 Defects in PBF-LB/M components

Despite the unique capabilities of the PBF-LB/M process, defects continue to be a major concern in metal components produced via additive manufacturing. This section offers a brief overview of the mechanisms behind defect formation and the strategies to mitigate some of the most challenging issues in components created using PBF-LB/M.

Numerous studies have investigated the effect of process parameters on microstructure, porosity levels, and defect formation. The influential process parameters include those related to the laser (such as laser power, spot size, pulse duration, and pulse frequency), scanning parameters (such as scanning speed, scan spacing or overlap, scan rotation, and scan pattern), powder-related parameters (such as powder morphology, particle size and distribution, layer thickness, dosage, and material properties), and macroscopic parameters (such as powder bed temperature and its uniformity, gas flow, gas type, and type of diffuser bar) [15]. Several factors contribute to the development of defects in PBF-LB/M.

Looking at the laser power and the scanning speed, it can be seen that at sufficiently high laser power, vapour-filled cavities, so-called "keyholes", are formed, which are likely to be unstable and lead to porosity above a certain threshold of power density. At constant laser power but increased scan speed, the keyhole becomes longer and shallower. In general, there is an optimal combination of power, speed, distance and depth between each pass. When considering constant power and velocity, the formation of humps leads to instability in the shape of the melt pool, which can result in porosity

formation. By increasing the scanning speed at constant power, incomplete fusion can occur where insufficient overlap of the melt pool causes unfused regions in the form of porosity or unfused particle inclusions. These defects can be illustrated in the figure 1.2 with respect to laser power and scanning speed [1]. The scanning strategy also plays a crucial role in controlling defect formation within the process. It impacts heat transfer, powder melting, and solidification rates, thereby influencing the types of defects that may occur.

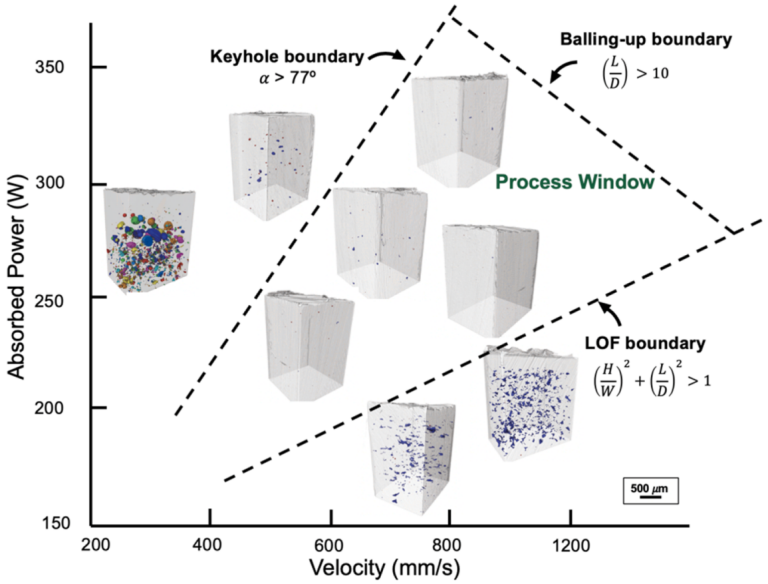

Figure 1.2: Morphologies of defects in relation to power and velocity [1].

Another defect that may manifest in PBF-LB/M is the *balling phenomenon*, typically observed under conditions of low laser power, high scanning speed, and a large layer thickness. The balling phenomenon presents several drawbacks in the quality of components produced through PBF-LB/M:

- it can lead to increased surface roughness of the part, in PBF-LB/M necessitating additional treatment for usability. These treatments not only add to costs but also result in a reduction in dimensional accuracy;
- it can cause a decrease in mechanical properties due to the formation of numerous pores between the metal balls;
- in severe cases, swollen metal balls tend to impede the movement of the roller, potentially causing scratching on unfinished parts [16].

To solve this problem, control methods such as increasing laser power, decreasing scan speed, reducing layer thickness, lowering the oxygen content in the atmosphere, adding a small amount of deoxidizer, and using laser re-fusion techniques can be implemented [17].

1.2.2 Design optimization of supports in PBF-LB/M

In fabricating components through PBF-LB/M, it is very important to provide additional structures to support the overhanging surfaces in order to minimize the geometric distortions that would result in layer-by-layer production of the component. These external structures are necessary, in addition to minimizing possible deformation, to anchor the part to the platform and to remove heat from the workpiece. This is especially helpful in components with internal channels and when workpiece overhangs are above a certain threshold. However, the use of these structures results in increased post-production machining and production of the part itself. Therefore, to improve process efficiency, efforts should be made to minimize support surfaces.

In order to minimize support structures, the component must be oriented to an optimal building position. This is usually done by identifying critical geometries, which in an PBF-LB/M process are usually the overhanging structures. They are considered critical because they are not supported by solidified material from the bottom layer during the construction of the object. It is precisely the orientation of the object that intervenes at this point, as a part of the component may or may not overhang depending on the orientation given to the component during its realization. Various solution algorithms have been developed to determine the orientation of the object. Once the orientation is determined, the object is defined using the xy-plane along the base of the construction platform and the z-axis along the construction direction [2].

In some cases, even when choosing the best orientation, it is not possible to avoid overhanging structures. When these structures are present, the main defect that occurs in the construction of the part is the staircase effect. In addition to dross formation and warp are also present. The stair effect occurs in that although PBF-LB/M is a very precise technique, the geometry can never match the exact geometry in the CAD file; it therefore turns out to be a stepped approximation of the 3D geometry.

In particular, it can be seen from the Fig.1.3 that at angles α, between the xy plane and the face of the wall, less than 30° the stair effect increases. Considering the angle α can be used to evaluate the criteria by which to identify a surface that is self-supporting and does not need a support structure and one that does. The literature indicates that surfaces with angles greater than 45° are self-supporting, whereas surfaces with angles up to 30° might not require support, depending on the size of their projection on the xy plane. For angles less than 30°, supports are always necessary. Additionally, surface roughness decreases as the angle increases, due to the reduced scale effect.

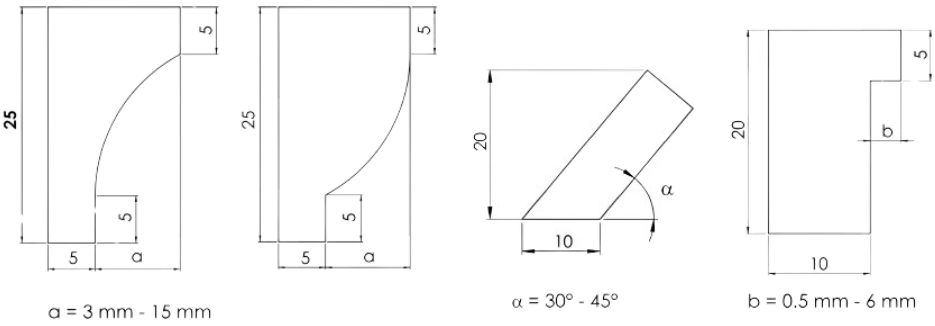

Figure 1.3: Self-supporting surfaces [2].

Downward-facing surfaces, such as overhangs, convex and concave radii, tend to deform due to gravity and capillary forces. During the construction of an PBF-LB/M component, rapid melting and cooling of the metal occur in localized areas. Material contraction during cooling leads to curling of the non-self-supporting material from the powder surface. For these geometries, support structures can be used to prevent deformation or collapse of the part during production.

1.3 Material analysis in the PBF-LB/M

This section examines the materials most commonly used in PBF-LB/M (Powder Bed Fusion using a Laser Beam in a Metallic material) that meet the requirements of the application discussed in this thesis. Each material is briefly described and its main properties are analyzed. There is also a summary table with the most important data, which provides an overview of the materials and helps to select the most suitable material for the application.

1.3.1 AlSi10Mg

AlSi10Mg is a good electrical conductor that avoids the issues encountered with pure aluminum or copper in PBF-LB/M. Post-production heat treatments reduce resistivity by 33% and eliminate variability due to the initial build orientation, making (AM) suitable for electrical applications.

Although PBF-LB/M is used with copper, silver, gold, and aluminum, the high costs of silver and gold limit their use to thin films, and pure copper is difficult to process with AM. Aluminum, despite having 60% higher resistivity than copper, is 30% lighter and cheaper, making it suitable for applications where weight or cost are critical, such as in the aerospace or automotive sectors. However, pure aluminum is too soft for manufacturing electric wires.

AlSi10Mg, an easily processable casting alloy for PBF-LB/M, has average hardness values of 1.54 GPa (as-built), 1.16 GPa (annealed), and 1.39 GPa (T6-like heat-treated). The samples analyzed in the article [18] showed that annealed and T6-like heat-treated samples had resistivities of 5.943 $\mu\Omega$-cm and 5.940 $\mu\Omega$-cm respectively, with no correlation between orientation and resistivity. In contrast, as-built samples showed resistivity variations based on orientation, with vertical builds at 7.78 $\mu\Omega$-cm, horizontal builds at 9.87 $\mu\Omega$-cm, and 45-degree builds at 9.01 $\mu\Omega$-cm.

The differences in microstructure, with Si forming cellular structures in the XY plane and elongated dendritic structures in the YZ plane, lead to anisotropic resistivity in as-built samples. Heat treatments break up Si-rich structures, allowing better electron pathways through Al, reducing resistivity.

Data on the resistivity of AlSi10Mg support its use in electrical applications and as a basis for new AM alloys. The design freedom offered by AM allows for creative solutions to overcome resistivity limitations. With ap-

propriate heat treatments, AM results in minimal resistivity penalties, with annealed and T6-like heat-treated samples showing comparable resistivities around 5.94 $\mu\Omega$-cm [18].

This alloy offers excellent strength and hardness, making it suitable for parts with thin walls and complex geometries subjected to high loads, such as those used in the aerospace and automotive industries.

The spherical morphology and smooth surface of the powder particles result in good flowability and uniform layer distribution. Due to the high thermal gradients in the PBF-LB/M process, parts are fabricated with high residual thermal stresses. To prevent the bending of AlSiMg parts during fabrication, it is essential to perform an stress relieving at 300 °C for 2 hours before removing them from the building platform. Stress relieving provides excellent dimensional and physical stability, as well as minimizing residual stresses. Cooling can be performed either in a furnace or in still air [5].

The following tables present the primary data for AlSi10Mg:

Element	**Si**	**Fe**	**Cu**	**Mn**	**Mg**	**Zn**	**Ti**
wt %	9 ÷ 11	≤ 0.55	≤ 0.05	≤ 0.45	0.2 ÷ 0.45	≤ 0.1	≤ 0.15

Table 1.1: Nominal composition of AlSi10Mg alloy powder [5].

Mateial	**Orientation**	**Yield strength [MPa]**	**Ultimate Tensile Strength [MPa]**	**Elongation at break [%]**
AlSi10Mg after PBF-LB/M	xy-plane	240 ± 8	330 ± 4	6.2 ± 0.4
	z-plane	230 ± 5	328 ± 4	4.1 ± 0.3

Table 1.2: Main values of tensile properties of AlSi10Mg for PBF-LB/M [5].

Condition	**Tensile Strength [MPa]**	**Yield Strength [MPa]**	**Elongation [%]**	**Hardness [HV]**	**Electrical conductivity [%IACS]**
AlSi10Mg AB	440	240 ± 8	6.2 ± 0.4	105 ± 5	25
AlSi10Mg T6	320	245	3.6	119	44

Table 1.3: Mechanical and electrical properties of AlSi10Mg before and after heat treatment [5, 4].

1.3.2 Scalmalloy®

PBF-LB/M has achieved significant success with several alloys, including titanium, aluminum, nickel, and steel. Among the Al-Si near-eutectic alloys, AlSi10Mg, Al-12Si, A357, and A356 are frequently used in PBF-LB/M processes, with AlSi10Mg being the most extensively researched. Its popularity is primarily due to the silicon content, which is close to the eutectic composition and minimizes cracking during manufacturing. Airbus introduced the first aluminum powder alloy specifically engineered for PBF-LB/M, named Scalmalloy®. This aluminum alloy incorporates magnesium and scandium as key elements. Although the mechanical properties can differ based on the machines and manufacturing conditions, Scalmalloy® heat-treated according to the manufacturer's guidelines (325°C for 4 hours) exhibits the highest yield strength, ultimate tensile strength, and elongation among aluminum alloys documented in the literature [6]. Similar to other metal components produced via PBF-LB/M, Scalmalloy® displays an anisotropic microstructure due to varying solidification rates and heat conductivity in different directions. Typically, heat conductivity along the building direction (Z-axis) is faster than in the X and Y axes, due to the efficient heat transfer of the pre-deposited metals.

Element		**Mg**	**Sc**	**Zr**	**Mn**
wt%	min	4.0	0.6	0.2	0.3
	max	4.9	0.8	0.5	0.8

Table 1.4: Nominal composition of Scalmalloy® [6].

From the analysis carried out in the article [6], it is noted that the Scalmalloy® alloy shows a bimodal microstructure with intergranular and intragranular precipitates. Immersion tests in NaCl indicate the formation of small pits without significant differences between the as-built and heat-treated samples. The heat-treated samples exhibit greater susceptibility to intergranular corrosion, although both are generally resistant.

Considering the heat treatment carried out after the component is produced by PBF-LB/M, some interesting changes in the mechanical and electrical properties of the component can be seen. Specifically, based on the analysis conducted in the article [19] it can be seen that the tensile testing of the samples in this study demonstrates significant alterations in mechanical

properties due to the implemented heat treatment. Specifically, the material's yield strength shows a notable increase from its initial state to after heat treatment, while Young's modulus remains relatively stable. Moreover, there is a distinct reduction in both the percentage of reduction of area and elongation, indicating a decrease in the material's ductility following treatment. These findings align with established research, suggesting that improvements in mechanical properties stem from the precipitation hardening effect brought about by the formation of secondary phases during the heat treatment process.

Regarding electrical properties the electrical conductivity measurements, performed according to ASTM E1004 standards, reveal that the heat-treated sample demonstrates a higher conductivity than the as-built sample.

The table 1.5 below shows the values obtained in the study [19]:

Condition	**Tensile Strength [MPa]**	**Yield Strength [MPa]**	**Elongation [%]**	**Hardness [HV]**	**Electrical conductivity [%IACS]**[3]
Scalmalloy® AB	349 ± 4	256 ± 4	20 ± 3	104 ± 2	20.47 ± 0.35
325°C for 4 h	509 ± 6	454 ± 3	11 ± 2	165 ± 3	23.94 ± 0.34

Table 1.5: Mechanical and electrical properties of Scalmalloy® before and after heat treatment.

[3]IACS: International Annealed Copper Standard

1.3.3 AlSi7Mg

AlSi7Mg is a hypoeutectic alloy that is widely used in the aerospace, automotive and marine industries due to its low density and excellent casting performance. PBF-LB/M offers greater machining freedom and efficiency and is therefore ideal for the production of complex AlSi7Mg components. The silicon content in AlSi7Mg is close to the eutectic point, which reduces the tendency to thermal cracking and improves its suitability for PBF-LB/M compared to other aluminum alloys. However, the conventional AlSi7Mg powder used in PBF-LB/M tends to oxidize, resulting in parts with lower mechanical properties and higher residual stresses. Researchers have addressed these issues through heat treatments and the development of ceramic-reinforced composites. stress relieving has been shown to significantly reduce the residual stress in AlSi7Mg [20].

The yield strength of AlSi7Mg alloy samples produced by PBF-LB/M improves in all three directions (xy, 45° and z) after T6 heat treatment. Initially, these samples exhibit a mixture of ductile and brittle fractures, which transitions to predominantly ductile fractures after heat treatment. Compared to AlSi10Mg and Al12Si, the AlSi7Mg parts formed by PBF-LB/M exhibit higher strength and better ductility. The heat treatment further improves the microstructure of the PBF-LB/M parts by promoting grain recrystallization, defect elimination and uniformity. After T6 treatment, the microstructure at the melt pool boundary remains as a eutectic Si network, but becomes discontinuous and forms chain-like particles. The PBF-LB/M AlSi7Mg alloy exhibits anisotropic tensile properties, with the T6 heat treatment improving the yield strength in all directions. Before heat treatment, the fracture mechanism includes ductile and brittle fractures in the xy and z directions and brittle fractures in the 45° direction. Post-treatment, it shifts to ductile fractures in the 45° and z directions, and a mix of ductile and brittle fractures in the xy direction [21].

In study [22], various thermal treatments were evaluated: stress relief (SR), low-temperature artificial aging (T5), and solution treatment followed by artificial aging (T6). These treatments significantly affect the alloy's microstructure:

- As-Built (AB): Features fibrous eutectic Si;

- T5: Shows abundant precipitation of Si nanocrystals within Al cells;
- SR: Si appears spheroidized and nearly homogeneously dispersed in the Al matrix;
- T6: Results in large Si plates homogeneously dispersed.

Thermal treatments impact conductivity by altering Si morphology. T5 and SR enhance conductivity compared to AB and T6 states, due to reduced lattice distortion and solute precipitation.

The following tables present the primary data for AlSi7Mg:

Element	**Si**	**Mg**	**Fe**	**Ti**
wt%	7.1	0.56	0.08	0.07

Table 1.6: Typical composition of AlSi7Mg [7].

Condition	**Tensile strength [MPa]**	**Yield strength [MPa]**	**Elongation [%]**	**Hardness [HV]**	**Electrical Conductivity [%IACS]**
AlSi7Mg AB	409.3± 1.5	236.0±0.0	15.3± 0.6	115	33.0
AlSi7Mg SR 280°C	246.0± 1.7	162.0±1.7	17.0± 1.7	80	47.0

Table 1.7: Mechanical and electrical properties of AlSi7Mg before and after heat SR treatment [8].

In article [8], the differences between the two materials are highlighted: AlSi7Mg exhibits slightly lower hardness compared to AlSi10Mg, and both materials experience a decrease in hardness following heat treatment. Conversely, heat treatment enhances the electrical conductivity of both AlSi10Mg and AlSi7Mg. Notably, AlSi7Mg demonstrates better electrical conductivity than AlSi10Mg. The electrical conductivity and mechanical properties of AlSi alloys are influenced by the precipitated Si content within the materials.

1.3.4 CuNi2SiCr

The low-alloyed copper alloy CuNi2SiCr is known for its thermal hardenability and high stiffness, even at elevated temperatures. CuNi2SiCr also boasts a balanced combination of electrical and thermal conductivity alongside exceptional wear resistance. The addition of nickel and silicon enhances its corrosion resistance, particularly against stress-corrosion cracking.

This distinctive set of properties makes CuNi2SiCr ideal for applications involving mechanical, thermal, or tribological stresses while maintaining good conductivity. It is commonly used in toolmaking, conductive contacts in electrical engineering, and valves. Components made from low-alloyed copper alloys using the PBF-LB/M process feature a homogeneous, nearly pore-free structure, ensuring mechanical properties that align with material specifications.

CuNi2SiCr crystallizes in a face-centered cubic lattice structure. The properties of the component can be tailored to specific requirements through subsequent heat treatment. Precipitation strengthening, which involves solution annealing, quenching, and artificial aging, enhances strength properties and increases electrical conductivity.

The following tables present the primary data for CuNi2SiCr taken from the datasheet [10]:

Element	**Ni**	**Si**	**Cr**	**Fe**	**Mn**	**Pb**
wt%	2.0 ÷ 3.0	0.5 ÷ 0.8	0.2 ÷ 0.5	0.15	0.1	0.02

Table 1.8: Nominal composition of CuNi2SiCr.

Condition	**Tensile strength [MPa]**	**Yield strength [MPa]**	**Elongation [%]**	**Hardness [HV]**	**Electrical Conductivity [%IACS]**
CuNi2SiCr AB	281	239	40	105	14
CuNi2SiCr heat-treated [4]	613	543	23	214	40

Table 1.9: Mechanical and electrical properties of CuNi2SiCr before and after heat treatment.

[4]Heat treatment involves solution stress relieving at 930 °C for 15 minutes, followed by water quenching. This is followed by aging at 540 °C for 2 hours, with subsequent cooling in air.

1.3.5 Cu-10Sn

The Cu-Sn alloy, known as tin bronze, is valued for its high mechanical properties, wear and corrosion resistance, and low shrinkage coefficient. Producing tin bronze components generally involves melting and casting, hot working, and cold working.

The PBF-LB/M process rapidly heats and cools the tin bronze, reducing segregation and refining the grain structure, thereby enhancing mechanical properties and density. However, the PBF-LB/M process faces challenges such as thermal residual stress, the spherical effect, and microstructural heterogeneity, which can limit part performance. Adjusting PBF-LB/M parameters and using heat treatments are common strategies to address these issues [9].

The article [23] shows that AB (as-built) specimens, regardless of orientation, exhibit similar compression strength, thermal conductivity, and corrosion properties. AB specimens have much higher compression strength than VA (vacuum annealing) specimens due to finer grain size and inter-phase interfaces. Additionally, the thermal conductivity of AB specimens is about 10-20% higher than that of specimens annealed at 800 ℃ and 600 ℃, due to the high thermal conductivity of the α phase. Heat treatment also significantly improves corrosion performance, reducing the corrosion rate by nearly 50% through modifications in passive layer morphology and reduced susceptibility to intergranular and internal galvanic corrosion.

The following tables present the primary data for Cu-10Sn:

Element	**Cu**	**Sn**	**P**	**Ni**	**Pb**	**Fe**	**Li**	**S**
wt%	90.2	9.5	0.24	0.012	0.0069	0.00044	0.0017	0.00094

Table 1.10: Typical powder composition of Cu-10Sn [9].

Condition	**Tensile strength [MPa]**	**Yield strength [MPa]**	**Elongation [%]**	**Hardness [HV]**	**Electrical Conductivity [%IACS]**
Cu-10Sn AB	435	302	13	122	11
Cu-10Sn 600°C x 4h	378	190	46	95	-

Table 1.11: Mechanical and electrical properties of Cu-10SN before and after heat treatment [9].

1.3.6 Summary and comparison of the materials

Below is a summary table outlining the key mechanical and electrical properties of the analyzed materials. This table is designed to facilitate comparison and provide insight into the most suitable materials for the application in question.

Material	**Condition**	**Tensile strength [MPa]**	**Yield strength [MPa]**	**Elongation [%]**	**Hardness [HV]**	**Electrical Conductivity [%IACS]**
AlSi10Mg	AB	440	240	6.2	105	25
	HT	320	245	3.6	119	44
Scalmalloy®	AB	349	256	20	104	20.47
	HT	509	454	11	165	23.94
AlSi7Mg	AB	409.3	236	15.3	115	33
	HT	246	162	17	80	47
CuNi2SiCr	AB	281	239	40	105	14
	HT	613	543	23	214	40
Cu-10Sn	AB	435	302	13	122	11
	HT	378	190	46	95	-

Table 1.12: Main properties of the materials analyzed; AB = As-Built, HT = Heat-Treated.

In the table above, it can be seen that the electrical conductivity, the main characteristic for the component discussed in this thesis, is greater in the materials AlSi10Mg, AlSi7Mg, and CuNi2SiCr. The highest conductivity values are always achieved following a specific heat treatment for each material. These materials also exhibit good mechanical properties, with CuNi2SiCr standing out among the three. For the application considered in this thesis, mechanical properties are important but not crucial, as the application is not subjected to significant loads or stresses. However, besides electrical conductivity, the weight of the component, and thus the density of the material used, is critical. Below is a table with the density values of these three materials:

Material	AlSi10Mg	AlSi7Mg	CuNi2SiCr
Density [g/cm^2]	2.67	2.64	8.84

Table 1.13: Density of the selected materials [4, 7, 10].

It can be observed that CuNi2SiCr has a significantly higher density compared to the other two materials. Therefore, the final material choice will be between AlSi10Mg and AlSi7Mg, which have very similar properties. AlSi7Mg

is slightly more electrically conductive and has a lower density, although it has inferior mechanical properties.

Chapter 2

Design and optimization of additively manufactured windings

This chapter will outline the sizing and design choices made for the development and modeling of the component that is the subject of this thesis: a tooth winding coil, drilled for the passage of coolant, manufactured using PBF-LB/M for a multi-three-phase surface permanent magnet motor. This winding will be mounted on a pre-existing motor, replacing the original winding. This is in order to change the supply voltage of the machine to 20 V. The following is a quick analysis of the original motor analyzed in the Ph.D. thesis [3] and then proceed to design the new winding.

2.1 Characteristics of the original motor

The original motor on which the winding subject of the thesis will be mounted is a multiphase surface permanent magnet motor intended for medium-low power traction applications. Multiphase motors were traditionally used to reduce the stator phase current in high-power applications; however, they are now also employed in traction applications due to their reliability, fault tolerance, weight and volume reduction, and high efficiency. Another major advantage is the ability to keep the electric drive operating even when one or more converter legs are not functioning properly.

A particular subset of multiphase drives is the multi-n-phase solution,

where the phases are grouped into separate stars of n-phases. The use of multi-star motors has shown immediate advantages in the past. In the event of a single star fault, these machines continue to operate with reduced performance and a decreased current ripple per phase unit. This solution is common in applications with high converter currents.

An additional advantage of this type of machine is found in the converter design, as this solution facilitates the integration of power converters and the active parts of motors from a cooling perspective. Dividing the current into different converter structures provides more space for power losses, achieving W/m^2 values similar to those typical of electric machines.

The motor was designed considering tooth coil windings, which are appreciated for their ease of construction and maintenance. However, choosing q=1 results in a significant harmonic contribution to the *Magneto Motive Force* (MMF). Therefore, fractional slot concentrated windings are commonly chosen. Thanks to the combination of a multiphase machine with tooth coil winding, it is possible to obtain a machine with a simple structure and a limited harmonic spectrum in the MMF.

The stator with concentrated winding offers performance benefits, such as simple construction, reduction of frontal connections and Joule losses, and the expansion of the constant power speed range due to the significant harmonic contribution of the MMF, which influences the stator inductance [24].

Among the multi-n-phase solutions, the multi-3-phase is one of the most interesting due to the availability of commercial 3-phase inverters. Considering all possible options, the design of this machine focuses on the solution that allows for the lowest number of slots, and for this reason, a triple-3-phase machine was selected [3].

Below, Table 2.1 shows the main data of the engine:

External diameter	142	mm
Air gap	0.5	mm
Active length	101	mm
PM remanence	1.2	T
Current density	13	A/mm^2
Number of 3-phase	3	-
Number of teeth	9	-
Number of PM	10	-

Table 2.1: Main data of the original motor.

The rotor, depicted in Fig. 2.1, of the motor features 10 slots for the motor's lightening and 10 slots for housing the magnets, which, since the motor is an SPM, are arranged along the motor's outer circumference and are kept hooked to the motor by an outer sealing ring and glue. Specifically, the magnets used for the application are NdFeB 38UH. These can have three main configurations:

- magnets with radial magnetization;
- magnets with parallel magnetization;
- array of magnets: 5 magnets side by side for each pole.

Although it is not the highest performance, the magnet array configuration was chosen because it reduces costs.

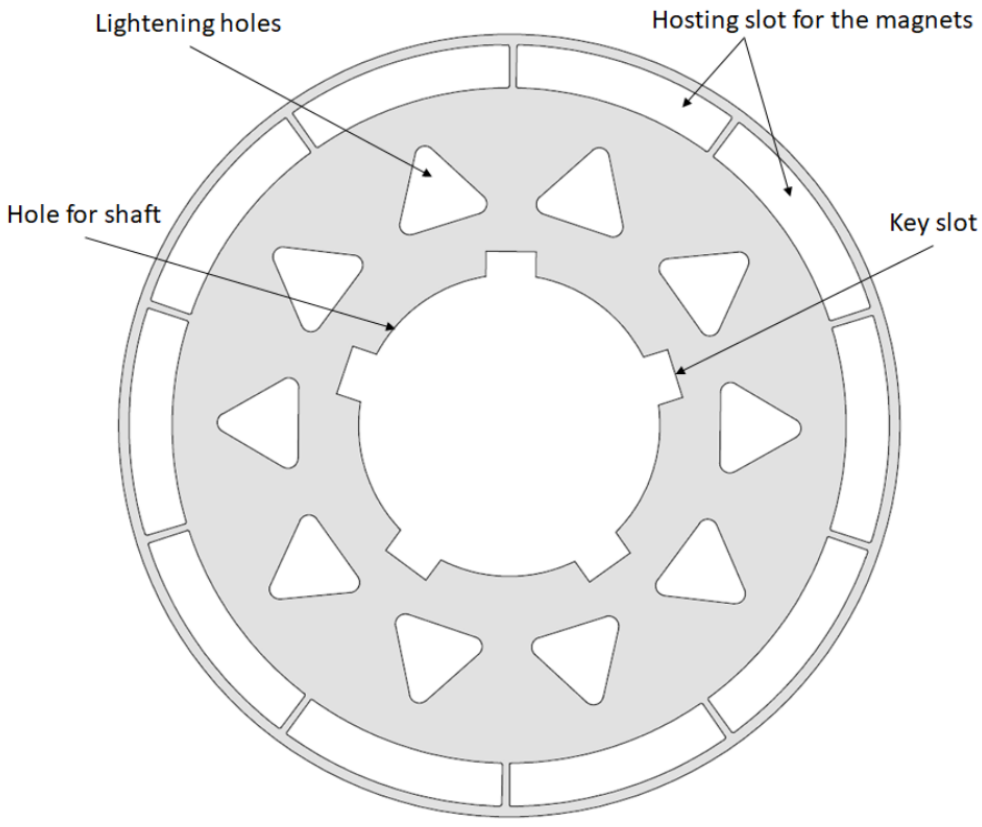

Figure 2.1: Representation of the rotor used [3].

Fig 2.2 below shows the main dimensions of the rotor:

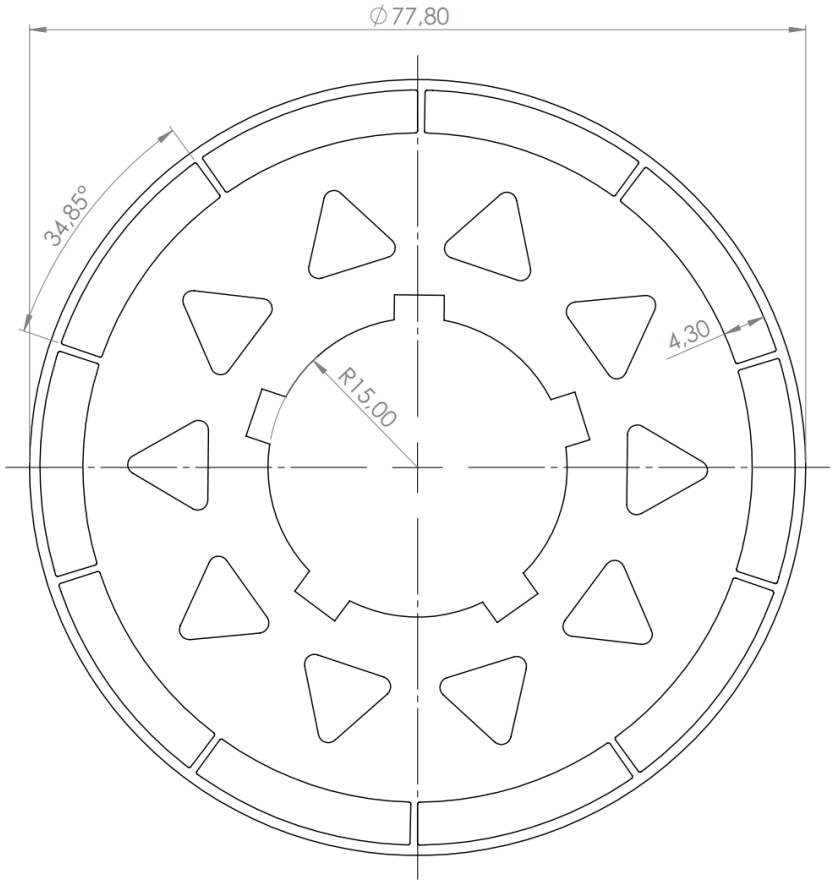

Figure 2.2: Main rotor dimensions expressed in $[mm]$.

The rotor and stator were constructed through *Electrical Discharge Machining* (EDM) using M250 35A pre-glued iron.

The stator consists of 9 teeth in which the concentrated windings that will form the three-phase triple motor will be housed. Where therefore each winding will correspond to a phase. Below, in Fig. 2.3, the stator section is shown, with the main dimensions:

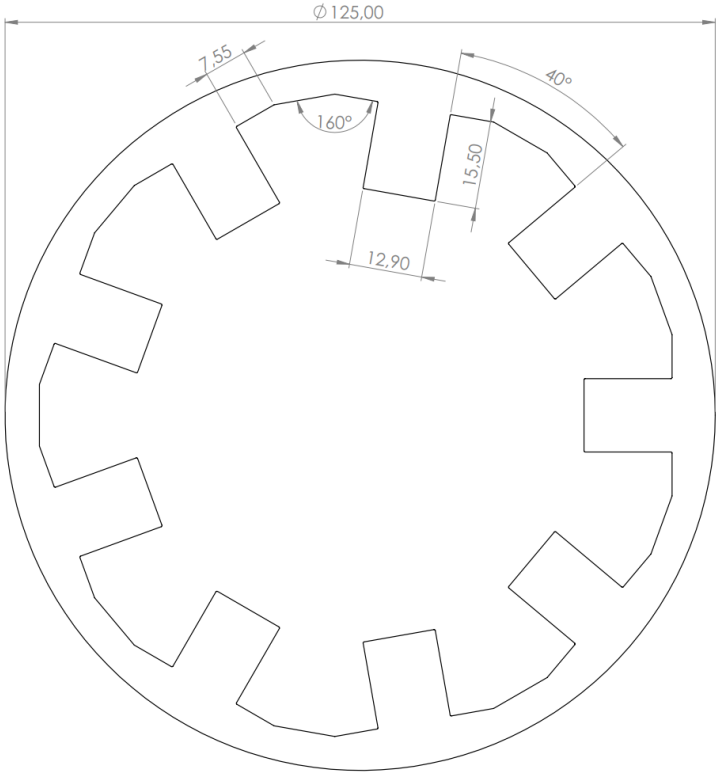

Figure 2.3: Main dimensions of the stator expressed in $[mm]$.

In the realization, the stator was subsequently placed inside the aluminum outer casing by interference thermal coupling. The stator made and placed inside the casing can be seen in Fig. 2.4 below:

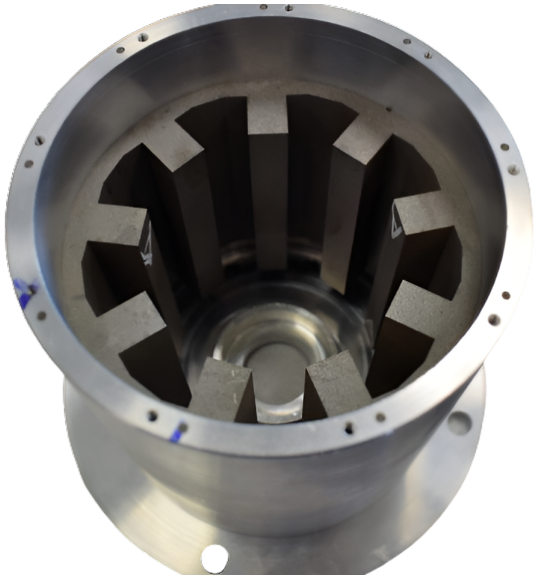

Figure 2.4: Stator inside the casing.

As mentioned earlier, the windings are made using a tooth coil configuration, created from nine preformed coils. These coils consist of copper enameled wire, also known as magnet wire, to improve the fill factor. Specifically, the tine coil is formed by a number of turns equal to 42 per coil. A sheet of Nomex was applied to the surface of the coil where it contacts the iron.

Figure 2.5: Coil views.

Finally in Fig. 2.6 the stator can be seen with the coils placed in the stator teeth.

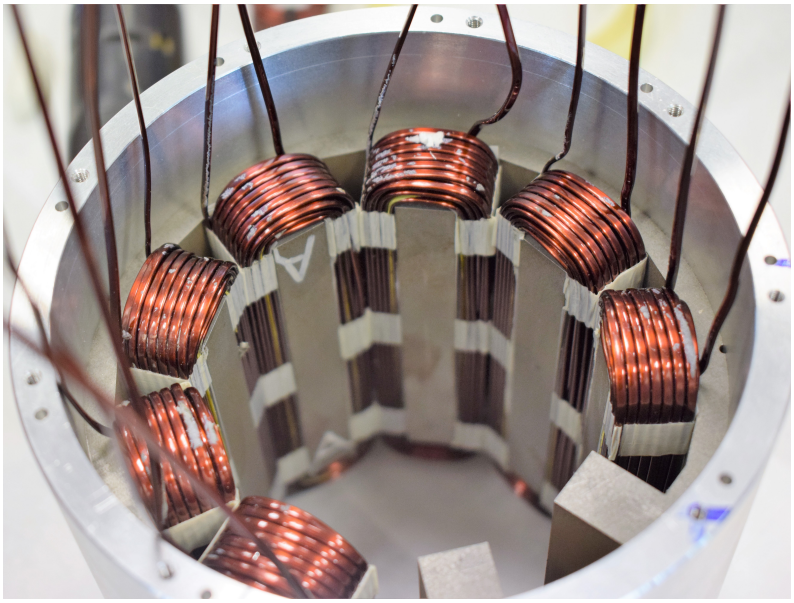

Figure 2.6: View of the stator with the coils placed.

2.2 Winding modifications and sizing

As described above, the preformed copper winding is replaced by a printed winding by additive manufacturing in order to change the maximum voltage at the DC-link from 400 V to 20 V.

To achieve this, the number of turns per coil was reduced from 42 to 4. Despite maintaining the same power output of 20 kW, this rewinding significantly increases the current, which in turn leads to substantial Joule losses. If these losses are not effectively managed, they could elevate the winding temperature to critical levels, potentially causing motor failure. Therefore, implementing a winding with 4 turns at 20V and a power of 20 kW for this application necessitates a specialized cooling solution. The approach developed in this thesis involves running coolant directly through the winding turns to maximize heat dissipation. Traditional metal processing technologies are inadequate for this solution due to the winding's small size and the complexity of creating the channel with a variable cross-section (as detailed later), through which the coolant will flow. Consequently, the winding will be manufactured using additive manufacturing, allowing for greater flexibility in designing and fabricating the internal cooling channels.

The design is focused on maximizing the slot fill, reducing the overall size of the winding heads, and creating a channel for the coolant to pass through. Although additive manufacturing allows for greater design flexibility, certain constraints must still be observed. Minimum thicknesses need to be maintained, and the curvatures, particularly those of the internal channel, should ideally be elliptical to ensure structural integrity during the construction process.

The winding sizing is shown below.

2.2.1 Winding sizing

The winding sizing was carried out starting from the dimensions of the stator, represented in Fig. 2.3. As previously mentioned, thanks to the great design freedom offered by AM production, different sections were chosen for each coil to maximize slot filling and obtain coil sections with as similar areas as possible, ensuring a uniform current density in each winding section. Specifically, the winding was considered to be divided frontally, and thus two different

sections were considered for each coil, as illustrated in Fig. 2.7.

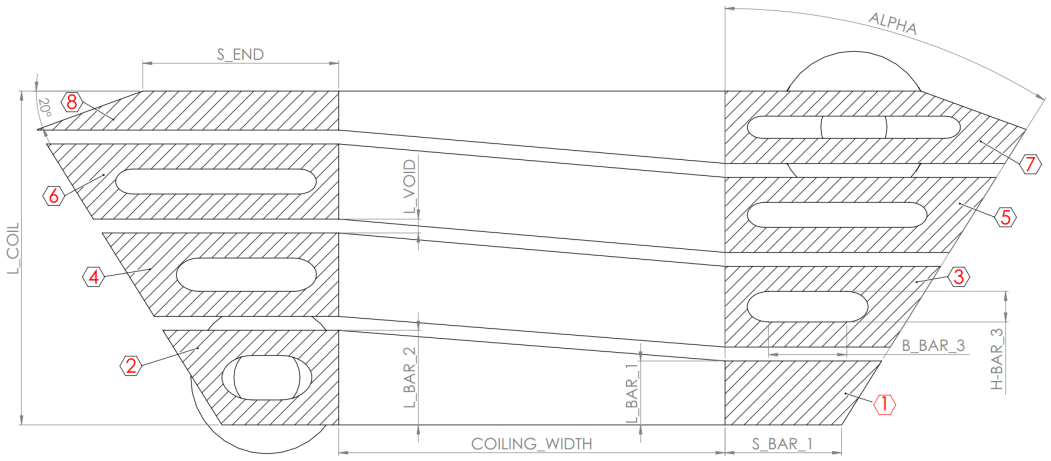

Figure 2.7: The main dimensions of the first version of the winding.

As can be seen from Fig. 2.7, the winding, which consists of 4 turns, has been divided into 8 sections with different shapes. These sections are numbered, starting with the section closest to the air gap and ending with the section closest to the stator yoke.

Each of these sections has been sized to achieve a constant area across the different sections, while maintaining the original design specifications, such as:

- total length of the stator tooth, L_SLOT;
- the width of the winding, TOOTH_WIDTH;
- the presence of a magnetic lamination occupying the last part of the tooth towards the air gap, L_LAMINATION;
- distance between each turn of 0.5 mm, L_VOID;
- distance between the winding and the stator of 0.5 mm, both vertically and horizontally, L_VOID;
- The length of the segment orthogonal to the stator tooth, before the stator hollow tilts, S_END;
- the depth of winding in the axial direction, WINDING_DEPTH.

The value of L_SLOT is easily obtained from the stator dimensions and corresponds to the length of the stator tooth, therefore:

$$\text{L\_SLOT} = 15.50\,mm \tag{2.1}$$

The distance between the various turns and between the winding and the stator is determined by design and is given by:

$$\text{L\_VOID} = 0.50\,mm \tag{2.2}$$

The magnetic lamination occupies a space of:

$$\text{L\_LAMINATION} = 3.00\,mm \tag{2.3}$$

From this data, the effective length of the winding can be calculated as:

$$\text{L\_COIL} = \text{L\_SLOT} - \text{L\_LAMINATION} - \text{L\_VOID} = 12.00\,mm \tag{2.4}$$

where L_VOID accounts for the distance of the winding from the stator yoke.

Another parameter that can be calculated is L_USEFUL, which corresponds to the sum of the heights of each section of the winding, i.e., the effective heights of the metallic material used for the winding. This is obtained considering that there are 3 voids between the turns, so:

$$\text{L\_USEFUL} = \text{L\_COIL} - 3 \cdot \text{L\_VOID} = 10.50\,mm \tag{2.5}$$

The value of TOOTH_WIDTH is obtained from the stator dimensions and corresponds to the width of the stator tooth, therefore:

$$\text{TOOTH\_WIDTH} = 12.90\,mm \tag{2.6}$$

From this value, the effective width of the winding can be calculated as:

$$\text{COILING\_WIDTH} = \text{TOOTH\_WIDTH} + 2 \cdot \text{L\_VOID} = 13.90\,mm \tag{2.7}$$

The winding depth in the axial direction can be calculated by taking the active length of the stator from Tab. 2.1 and taking into account the distance

between the winding and the stator tooth in the axial direction, therefore:

$$\text{WINDING\_DEPTH} = \text{Active\_length} + 2 \cdot \text{L\_VOID} = 102.00\,mm \tag{2.8}$$

The value of S_END is obtained from the stator dimensions in Fig. 2.3 and therefore always takes into account the distance between the winding and the stator tooth, therefore:

$$\text{S\_END} = 7.55\,mm - \text{L\_VOID} = 7.05\,mm \tag{2.9}$$

The results obtained are summarized in Tab. 2.2:

L_SLOT	15.50	mm
L_VOID	0.50	mm
L_LAMINATION	3.00	mm
L_COIL	12.00	mm
L_USEFUL	10.50	mm
TOOTH_WIDTH	12.90	mm
COILING_WIDTH	13.90	mm
S_END	7.05	mm
WINDING_DEPTH	102.00	mm

Table 2.2: Fixed design values.

As previously mentioned, the winding has been divided into 8 sections, each of which has different dimensions. These dimensions can be defined as:

- S_BAR_i is the base width of the i-th section, with $i = 1, 2, ..., 8$;
- L_BAR_i is the height of the i-th section;
- B_BAR_i is the cavity width of the i-th section, excluding the first and the eighth sections;
- H_BAR_i is the cavity height of the i-th section, excluding the first and the eighth sections;
- ALPHA is the angle of inclination of the outer part of the winding.

Only S_BAR_1, S_BAR_2, and ALPHA are fixed in order to allow maximum cavity filling and simultaneously enable the insertion of two windings into the same cavity without interference. The assigned values are:

- S_BAR_1 = 4.20 *mm*;
- S_BAR_2 = 4.20 *mm*;
- ALPHA = 32°.

All other dimensions are calculated accordingly, except for L_BAR_i. For L_BAR_i, the sum of the values for even indices must equal L_USEFUL, and similarly, the sum of the values for odd indices must meet the specified total. These values are then determined using a spreadsheet (e.g., Excel), adjusting them to make the areas of the sections as similar as possible while adhering to the minimum allowable thickness of 0.8 mm for construction via PBF-LB/M. Since variations in L_BAR_i impact the calculation of all other dimensions, as will be emphasized below, it is practical to use a spreadsheet to compute the values for the various dimensions efficiently.

Here are the equations used in the spreadsheet to define the dimensions of the winding sections:

The S_BAR_i values are derived from geometric constructions, being influenced by the angle ALPHA through the following equation:

$$\text{S\_BAR\_i} = \text{S\_BAR\_(i} - 2) + \left((\text{L\_BAR\_(i} - 2) + \text{L\_VOID}) \cdot \tan\left(\text{ALPHA} \cdot \frac{\pi}{180}\right)\right) \quad \text{per } i = 3, \ldots, 8 \tag{2.10}$$

The height of the channel slot for the passage of the cooling fluid is calculated in such a way as to maintain a wall thickness of 0.9 mm, resulting in:

$$\text{H\_BAR\_i} = \text{L\_BAR\_i} - (2 \cdot 0.9) \quad \text{per } i = 2, \ldots, 7 \tag{2.11}$$

The width of the groove is calculated by taking into account the elliptical curvature of the groove, which will be described in more detail later, and the minimum wall thickness of 0.8 mm, resulting in:

$$\text{B\_BAR\_i} = \text{S\_BAR\_i} - (2 \cdot 0.7 \cdot \text{H\_BAR\_i} + 2 \cdot 0.8) \quad \text{per } i = 2, \ldots, 7 \tag{2.12}$$

Below, in Tab. 2.3, are listed all the dimension values used in the winding modeling, extracted from the spreadsheet.

Dimension	**Value**	**Units**	**Dimension**	**Value**	**Units**
L_BAR_1	2.30	*mm*	**S_BAR_1**	4.20	*mm*
L_BAR_2	3.40	*mm*	**S_BAR_2**	4.20	*mm*
L_BAR_3	2.90	*mm*	**S_BAR_3**	5.95	*mm*
L_BAR_4	3.00	*mm*	**S_BAR_4**	6.64	*mm*
L_BAR_5	2.70	*mm*	**S_BAR_5**	8.07	*mm*
L_BAR_6	2.70	*mm*	**S_BAR_6**	8.82	*mm*
L_BAR_7	2.60	*mm*	**S_BAR_7**	10.07	*mm*
L_BAR_8	1.40	*mm*	**S_BAR_8**	10.82	*mm*
-	**-**	*mm*	**S_END**	7.05	*mm*
Dimension	**Value**	**Units**	**Dimension**	**Value**	**Units**
-	-	*mm*	**-**	-	*mm*
H_BAR_2	1.60	*mm*	**B_BAR_2**	1.00	*mm*
H_BAR_3	1.10	*mm*	**B_BAR_3**	2.81	*mm*
H_BAR_4	1.20	*mm*	**B_BAR_4**	3.36	*mm*
H_BAR_5	0.90	*mm*	**B_BAR_5**	5.21	*mm*
H_BAR_6	0.90	*mm*	**B_BAR_6**	5.96	*mm*
H_BAR_7	0.80	*mm*	**B_BAR_7**	6.55	*mm*
-	**-**	*mm*	**-**	**-**	*mm*
-	**-**	*mm*	**-**	**-**	*mm*

Table 2.3: Main value of winding sections.

To simplify the design, it was decided not to drill all 8 sections. Specifically, section 1 and section 8, which correspond to the electrical connections (power supply for the phase and the closure of the neutral point of the three-phase system), were not drilled. The remaining six sections, however, were drilled to allow the coolant to flow through them. For this application, a simple circular hole was insufficient, as it would cover too small an area and thus provide inadequate heat exchange. A rectangular hole was also unsuitable due to manufacturing challenges with PBF-LB/M, as the structure would not be self-supporting. Additionally, a near-rectangular hole with circular shorter sides was not feasible, as it too would not be self-supporting.

Therefore, the solution chosen was a nearly rectangular hole with elliptical short sides, as can be seen in Fig. 2.8, to ensure that the structure would remain self-supporting during fabrication by PBF-LB/M. The equations used to construct this type of groove are described below:

The semi-axis a_i is given by:

$$\text{a\_i} = 0.7 \cdot \text{H\_BAR\_i} \quad \text{per } i = 2, \ldots, 7 \tag{2.13}$$

While the semi-axis b_i is given by:

$$\text{b\_i} = 0.5 \cdot \text{H\_BAR\_i} \quad \text{per } i = 2, \ldots, 7 \tag{2.14}$$

The tunnel area in each section is calculated as:

$$\text{TUNNEL\_AREA\_i} = \text{B\_BAR\_i} \cdot \text{H\_BAR\_i} + (\pi \cdot \text{a\_i} \cdot \text{b\_i}) \quad \text{per } i = 2, \ldots, 7 \tag{2.15}$$

Figure 2.8: Schematic of the groove.

Below, in Tab. 2.4, the values of the ellipse semi-axes for constructing the grooves in the winding sections are provided.

Dimension	Value	Units	Dimension	Value	Units
a_2	1.12	*mm*	**b_2**	0.8	*mm*
a_3	0.77	*mm*	**b_3**	0.55	*mm*
a_4	0.84	*mm*	**b_4**	0.60	*mm*
a_5	0.63	*mm*	**b_5**	0.45	*mm*
a_6	0.63	*mm*	**b_6**	0.45	*mm*
a_7	0.56	*mm*	**b_7**	0.4	*mm*

Table 2.4: Main value of the groove sections.

In Table 2.5, the values of the groove areas for each winding section are provided.

Dimension	Value	Units
TUNNEL_AREA_2	4.41	mm^2
TUNNEL_AREA_3	4.42	mm^2
TUNNEL_AREA_4	5.61	mm^2
TUNNEL_AREA_5	5.58	mm^2
TUNNEL_AREA_6	6.26	mm^2
TUNNEL_AREA_7	5.95	mm^2

Table 2.5: Tunnel values in the sections.

In addition to what has already been described, there is another specification regarding the geometry of the winding sections. Specifically, in sections 7 and 8, due to the geometry of the stator slot and the need to maximize the slot fill as much as possible, it is necessary to create a geometry that follows the profile of the stator slot, as shown in Fig. 2.9.

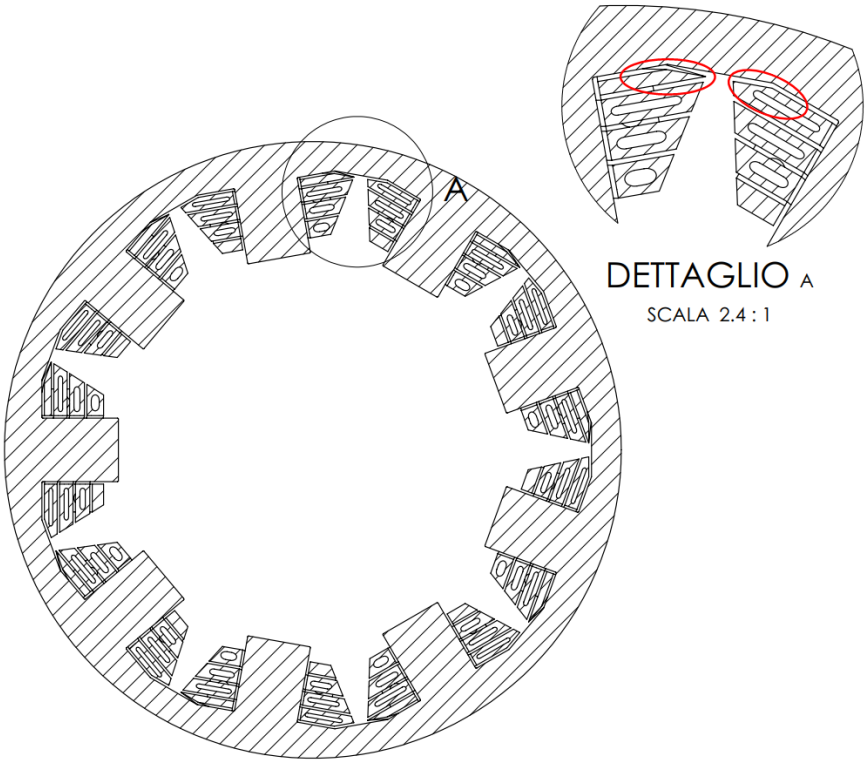

Figure 2.9: Triangles to be subtracted from winding.

Therefore, in the section calculations, it was necessary to create a triangle to "subtract" from the geometry, visible in Fig. 2.10, previously described. The calculations used are given below:

$$\beta = 180^\circ - \alpha - 70^\circ = 78^\circ \tag{2.16}$$

At this point, it is possible to calculate the data of the triangle under analysis, the red one in Fig. 2.10. PStarting from the angles that are calculated as:

$$\beta_{tri} = 90^\circ - 70^\circ = 20^\circ \tag{2.17}$$

$$\gamma_{tri} = 90° - \alpha = 58° \tag{2.18}$$

$$\alpha_{tri} = 180° - \beta_{tri} - \gamma_{tri} = 102° \tag{2.19}$$

It is now possible to calculate the sides of the triangle using the Law of Sines:

$$\frac{a_{tri}}{\sin(\alpha_{tri})} = \frac{b_{tri}}{\sin(\beta_{tri})} = \frac{c_{tri}}{\sin(\gamma_{tri})} \tag{2.20}$$

$$a_{tri} = l \cdot \tan(32°) - (\text{S\_END} - \text{S\_BAR\_1}) = 4.65\,mm \tag{2.21}$$

$$b_{tri} = \frac{a_{tri}}{\sin(\beta_{tri})} \cdot \sin(\gamma_{tri}) = 1.63\,mm \tag{2.22}$$

$$c_{tri} = \frac{a_{tri}}{\sin(\alpha_{tri})} \cdot \sin(\gamma_{tri}) = 4.03\,mm \tag{2.23}$$

It is therefore possible to calculate the area of the triangle as:

$$Area_{tri} = \frac{1}{2} \cdot b_{tri} \cdot c_{tri} \cdot \sin(\alpha_{tri}) = 3.20\,mm^2 \tag{2.24}$$

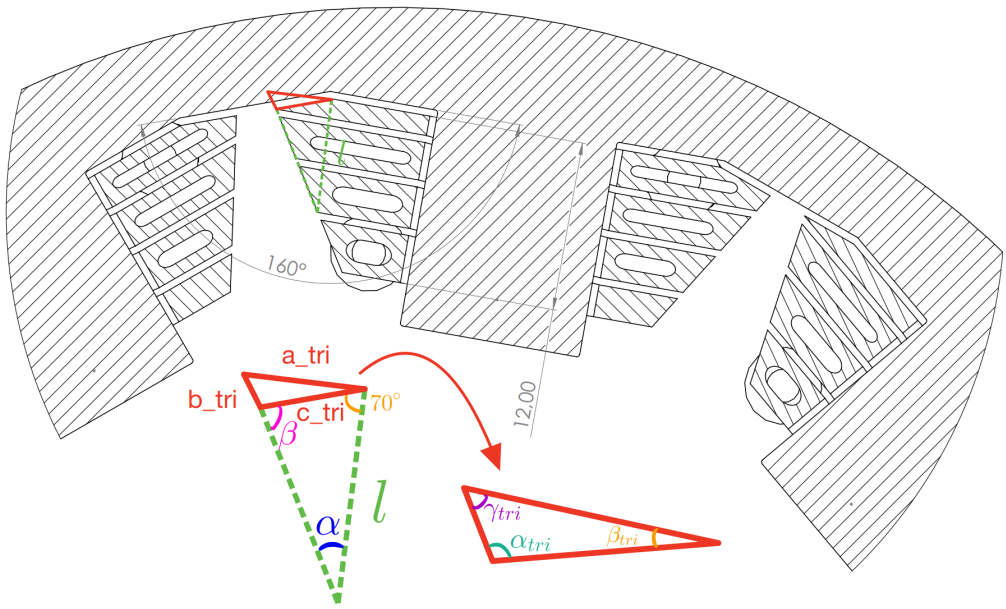

Figure 2.10: Triangle dimensions to be subtracted from winding.

The calculated values for the triangle are listed in Tab. 2.6 below:

Dimension	**Value**	**Units**
a_{tri}	4.65	mm
b_{tri}	1.63	mm
c_{tri}	4.03	mm
α_{tri}	102	deg
β_{tri}	20	deg
γ_{tri}	58	deg
$Area_{tri}$	3.20	mm^2

Table 2.6: Triangle dimensions.

At this point, it is possible to calculate the effective conductor material areas for each winding section, which will be given by the following equations:

$$\begin{aligned}\text{Area}_i &= \text{S\_BAR\_i} \cdot \text{L\_BAR\_i} + \frac{1}{2} \cdot \text{L\_BAR\_i} \cdot \left(\text{L\_BAR\_i} \cdot \tan\left(\alpha \cdot \frac{\pi}{180°}\right)\right) \\ &= 11.31\,\text{mm}^2 \quad \text{per } i = 1\end{aligned} \tag{2.25}$$

$$\begin{aligned}\text{Area}_i = \text{S\_BAR\_i} \cdot \text{L\_BAR\_i} + \frac{1}{2} \cdot \text{L\_BAR\_i} \cdot \left(\text{L\_BAR\_i} \cdot \tan\left(\alpha \cdot \frac{\pi}{180°}\right)\right) - \text{TUNNEL\_AREA\_i} \\ \text{per } i = 2, \ldots, 6\end{aligned} \tag{2.26}$$

$$\begin{aligned}\text{Area}_i &= \text{S\_BAR\_i} \cdot \text{L\_BAR\_i} + \frac{1}{2} \cdot \text{L\_BAR\_i} \cdot \left(\text{L\_BAR\_i} \cdot \tan\left(\alpha \cdot \frac{\pi}{180°}\right)\right) \\ &\quad - \text{TUNNEL\_AREA\_i} - \text{Area}_{tri} \quad \text{per } i = 7, 8\end{aligned} \tag{2.27}$$

Below, Tab. 2.7 shows the values of the actual conducting areas of the winding.

Dimension	**Value**	**Units**
$Area_1$	11.31	mm^2
$Area_2$	13.48	mm^2
$Area_3$	15.46	mm^2
$Area_4$	17.11	mm^2
$Area_5$	18.49	mm^2
$Area_6$	19.48	mm^2
$Area_7$	19.15	mm^2
$Area_8$	12.56	mm^2

Table 2.7: Effective areas of the conductor sections of the winding.

2.3 Realization by 3D CAD

The CAD modeling of the winding was carried out using the parametric 3D design and drawing software, Solidworks. This allowed for an initial digital representation of the winding and a quick check of the space within the stator, as well as the possibility of inserting a winding into a slot adjacent to one already occupied by another winding. Furthermore, the CAD design is necessary to obtain the STL file, which will then be uploaded to the machine for PBF-LB/M printing.

As shown in Figs. 2.11 and 2.12, the part of the winding intended for electrical connections can be observed. Specifically, the adopted solution was to create two vertical tabs with a 2.5 mm hole, to which a PCB (*Printed Circuit Board*) will be connected. This PCB will manage the winding's power supply and the closure of the star center. Since the selected motor is a three-phase triple motor, each phase will have its own power supply and there will be a total of three star centers, one for each three-phase. The solution with the PCB was chosen because it allows for the simplest and most compact management of these electrical connections.

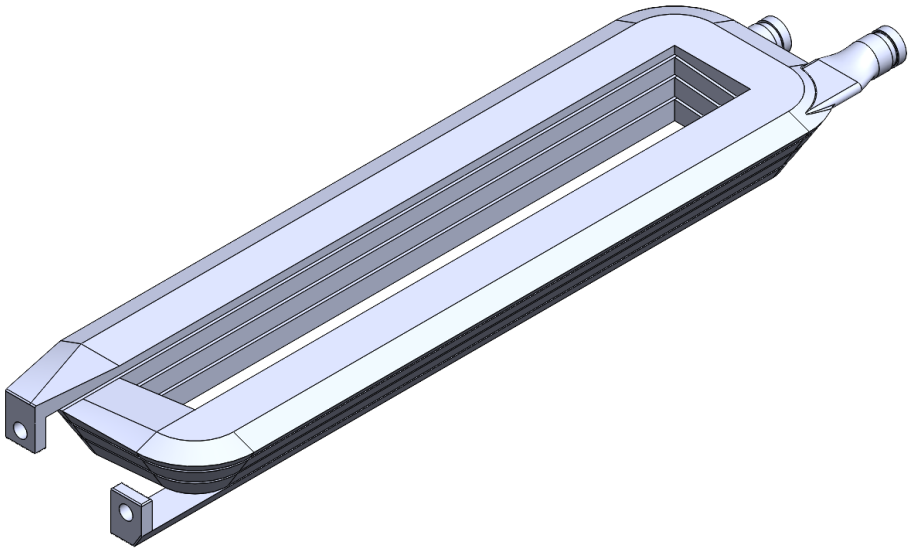

Figure 2.11: Electrical isometric view of the winding.

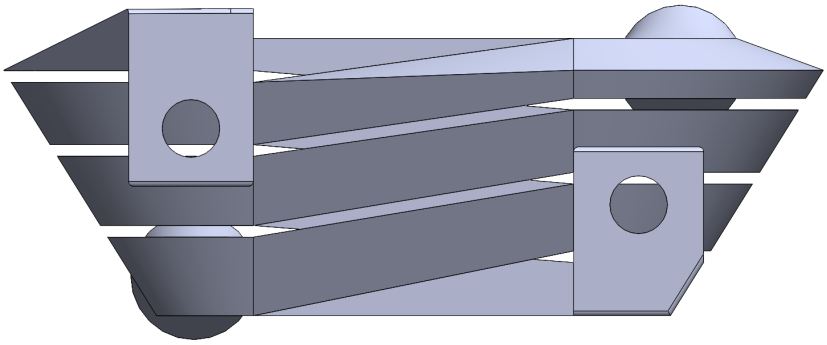

Figure 2.12: Electrical front view of the winding.

In figures 2.13 and 2.14, the view of the hydraulic connection part of the winding is shown. Specifically, to connect the coolant pump to the winding, allowing the coolant, in this case 50% water and 50% glycol, to flow through the grooves created within the winding, two perforated cylinders were created. These will be connected to a fluid manifold, described later, which will be linked to the pump. The images show the circumferential grooves created in these cylinders, which will house the O-rings responsible for sealing the connection between the winding's hydraulic system and the coolant manifold. These cylinders were "connected" to the winding structure in the CAD design using the *loft* function, allowing for a gradual variation in the cavity section to minimize turbulence in the coolant flow. For the same reason, fillets were applied at the entrance of the cylinder cavities.

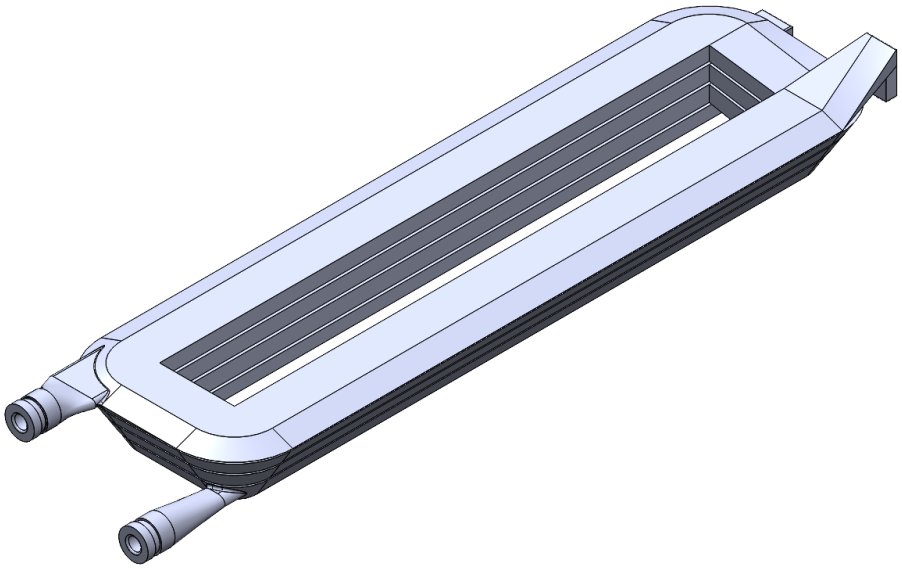

Figure 2.13: Hydraulic isometric view of the winding.

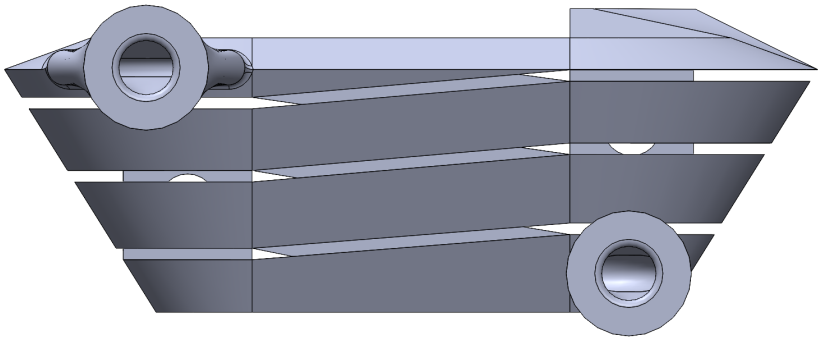

Figure 2.14: Hydraulic front view of the winding.

The sections described in Paragraph 2.2.1 correspond to the active sides of the winding, however, these must be connected in such a way as to form the winding itself. Since all 8 sections are different, the front connection, visible in section in Fig. 2.15, between one section and another will consist of a variable section that allows the connection of the two sections and at the same time allows the fluid to flow without encountering sudden variations that could lead to turbulence. For this reason, the cavity inside does not follow a perfect rectangular path as the vertices of the ideal rectangle have been rounded.

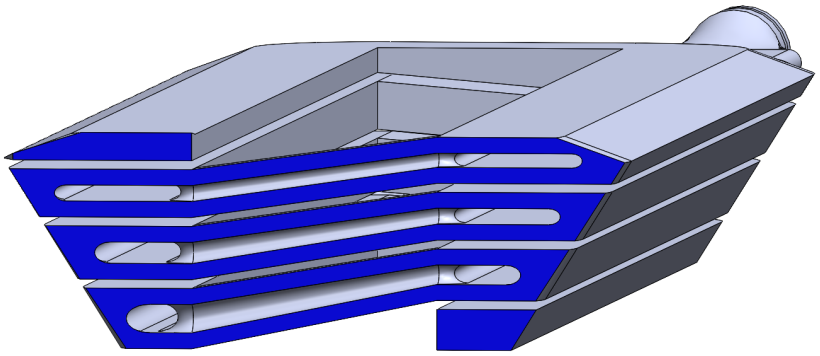

Figure 2.15: View of front winding connections.

Below, in Fig. 2.16, the main dimensions (in *mm*) of the winding and the measurements of the electrical and hydraulic connections, as well as their respective holes, are shown.

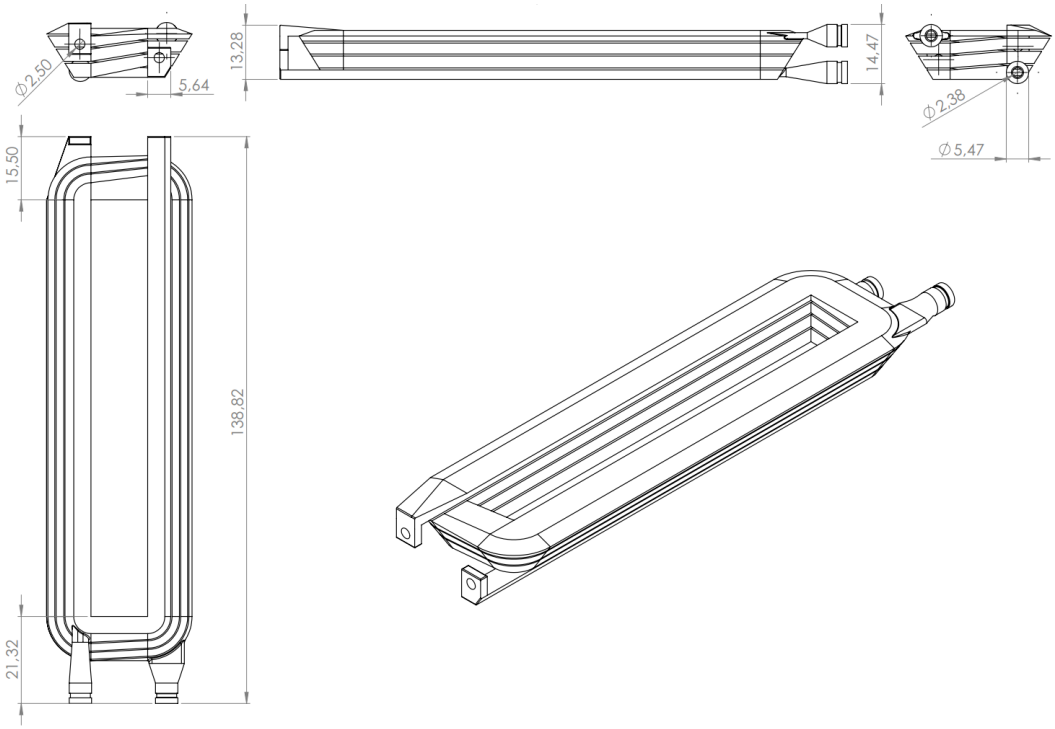

Figure 2.16: Views and dimensions of the winding.

2.4 3D representation of the motor

In this section, the engine is depicted with its main components, represented in different colors only to facilitate their distinction, in order to provide a better understanding of the layout of the windings and hydraulic connections. Specifically, the rotor is shown in red, the stator in green, the windings in gray, and the coolant fluid manifold in yellow. In Fig. 2.17, an isometric view of the electrical side of the engine is shown.

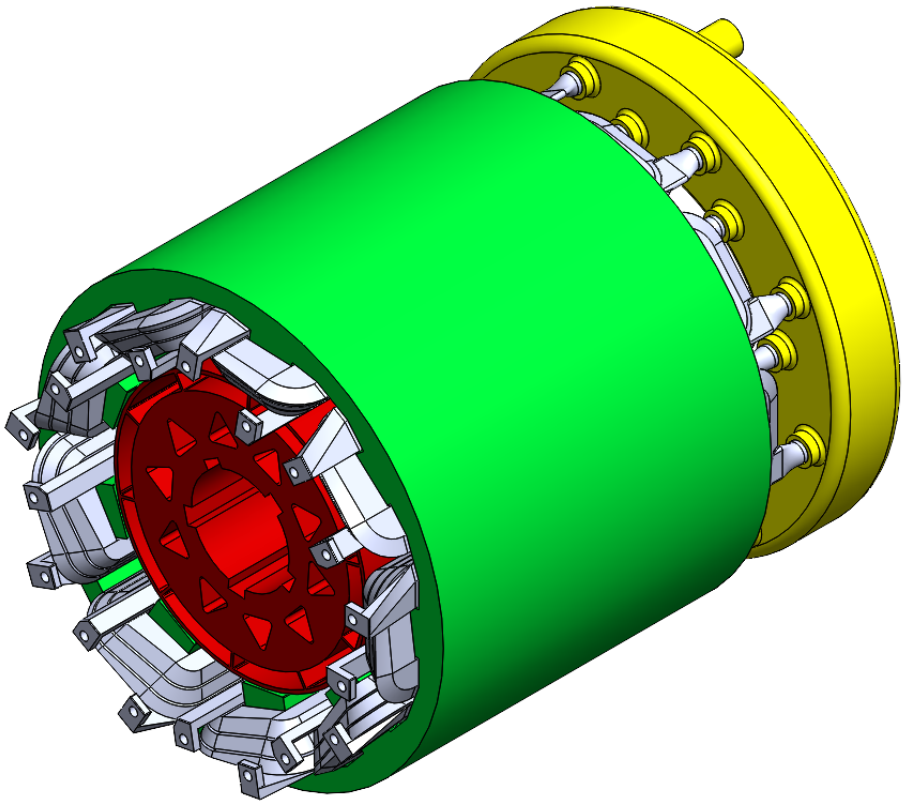

Figure 2.17: Isometric view of the electrical side of the motor.

In Fig. 2.18 below, the front view of the electrical side of the engine is shown. From this view, it can be observed how the connections to the electrical terminals are arranged in two different circumferences. On the outer circumference, through the PCB, the connection to the winding power supply is made, while on the inner circumference, the star centers of the three-phase sets are closed.

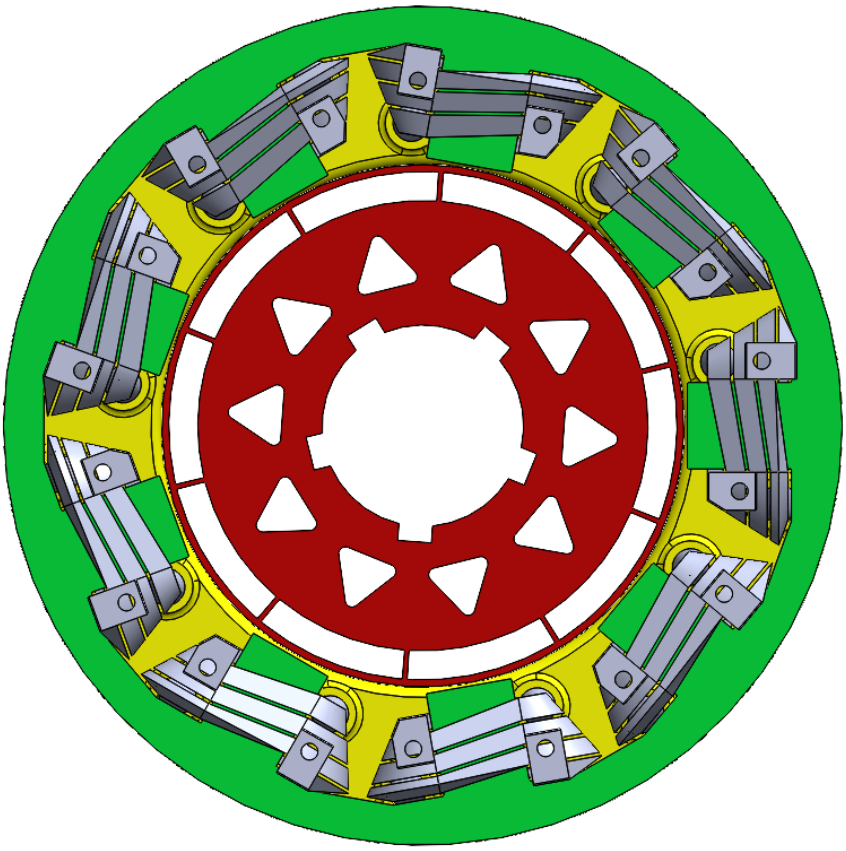

Figure 2.18: Front view of the electrical side of the motor.

Below, in Fig. 2.19, the isometric view of the hydraulic side of the engine is shown. It can be observed that the hydraulic manifold (depicted in yellow in the figure) has two connections for the inlet/outlet of the coolant. Specifically, the lower protrusion will be connected to the pump's supply, representing the inlet of the low-temperature coolant, while the upper protrusion represents the outlet of the coolant, which will have absorbed the heat produced by the windings and will then need to be cooled in the radiator before returning to the pump.

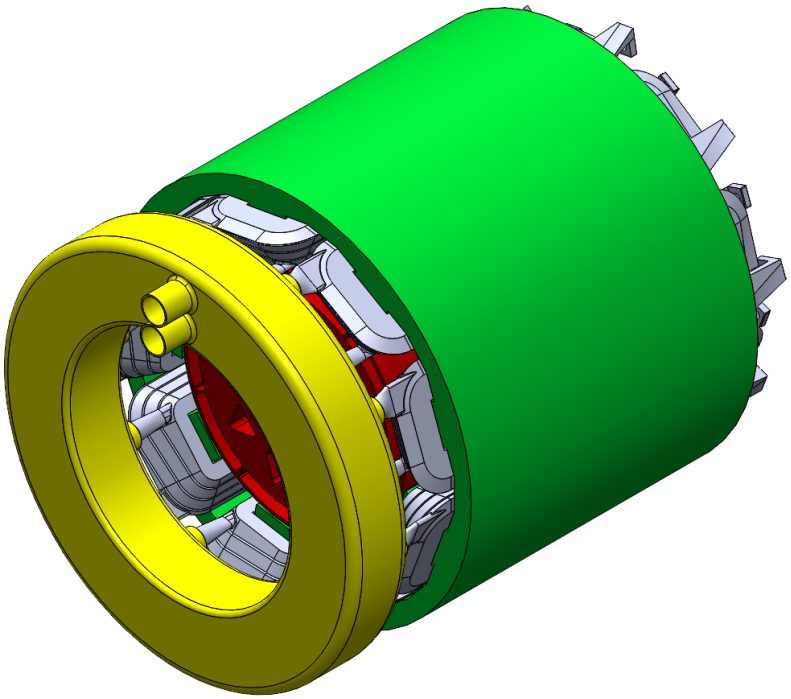

Figure 2.19: Isometric view of the hydraulic side of the motor.

In Fig. 2.20, the engine is shown in an exploded view to highlight the connections between the hydraulic manifold and each individual winding. The manifold is inserted into the hydraulic terminals of the winding, and the seal is ensured by O-rings.

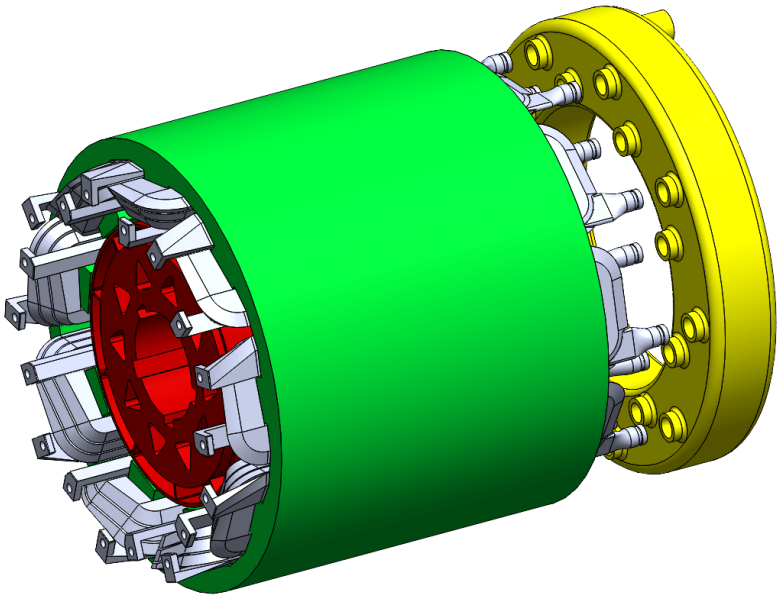

Figure 2.20: Exploded view of the hydraulic manifold.

Below, in Fig. 2.21, the engine is shown with a sectioned view of the hydraulic manifold to highlight the two circular chambers inside it. From the two main inlets visible in Fig. 2.19, the coolant enters through the lower protrusion, fills the inner circular chamber, and is then distributed to all the windings. After flowing through the coils of each winding, the coolant is collected in the outer circular chamber and exits the manifold through the upper protrusion, directed towards the radiator before re-entering the pump and starting the cycle again.

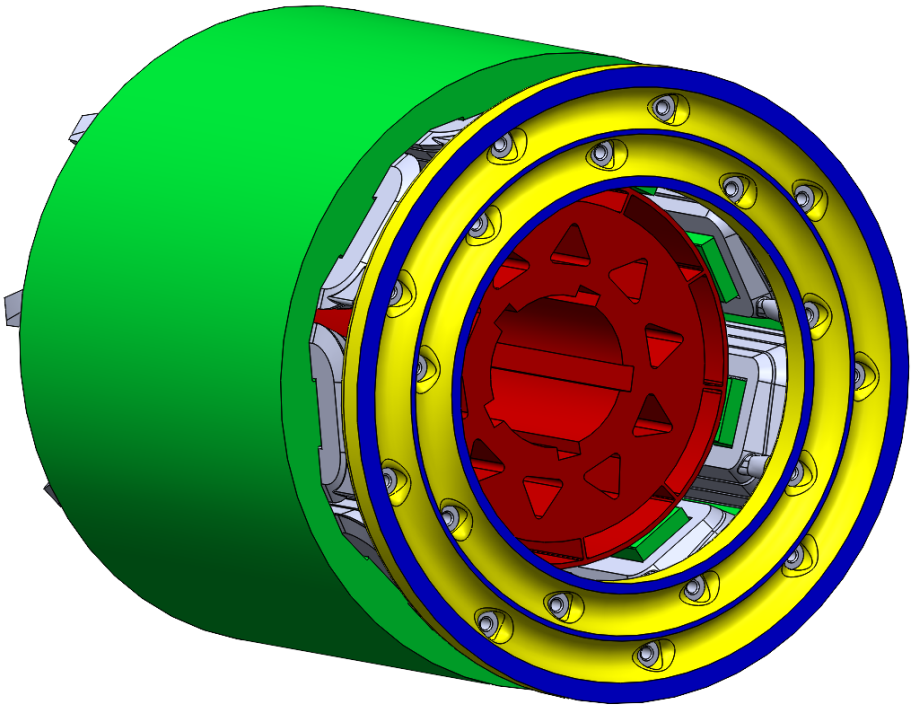

Figure 2.21: View of the engine with the sectioned manifold.

Chapter 3

Realization through PBF-LB/M and results

In this chapter of the thesis, the main features of the two prints carried out on the first version of the winding are described. A brief description of the machinery used and the powders employed for printing is provided. Two prints were made, one in pure copper and one in AlSi10Mg aluminum, in order to test the winding and compare the results with those obtained in Chapter 5 through the COMSOL software.

As described in Chapter 1, in order to proceed with printing, the CAD file of the part to be printed must be converted into an STL file (Standard Tessellation Language) and then uploaded to the PBF-LB/M machine, which will handle the printing of the object. The machine used for both prints was the EOSINT M 270 from EOS.

3.1 Copper printing of the winding

The first print was made in pure copper, using metal powder from LPW. Although it was not recommended, it was necessary to perform two refills during the printing process. In Fig. 3.1 , the part can be seen in the printing chamber following the completion of the printing process, with the residual copper powder that needs to be removed.

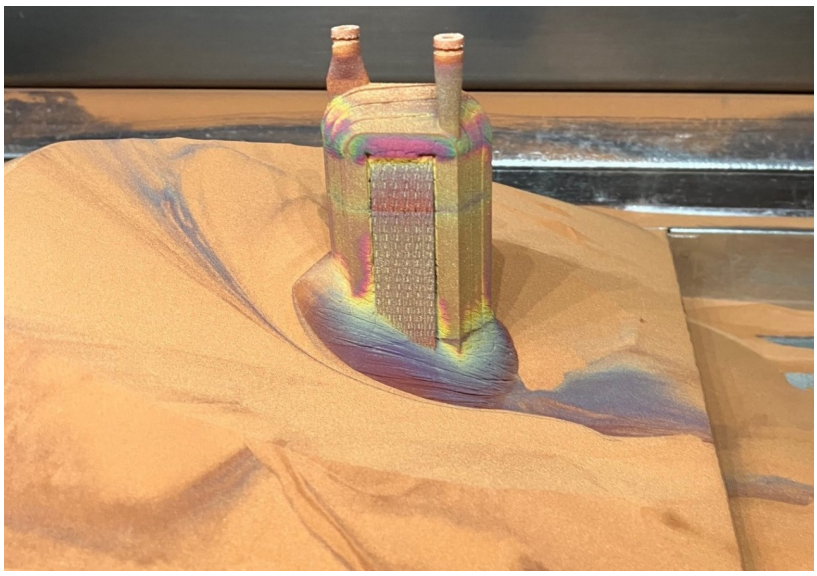

Figure 3.1: Printing in pure copper of the first version of the winding.

The figure shows that the part was built vertically, using the electrical section of the winding as a base, and constructing it along its greater length. This was done to minimize supports, as in this orientation the part is self-supporting during printing with the fewest number of supports.

Additionally, a particular coloration of the part can be observed. This coloration is even more evident in Fig. 3.2, which also reveals a certain fragility of the obtained piece. Notably, a well-defined line can be seen at about half the height of the winding, and one of the two hydraulic connections has failed.

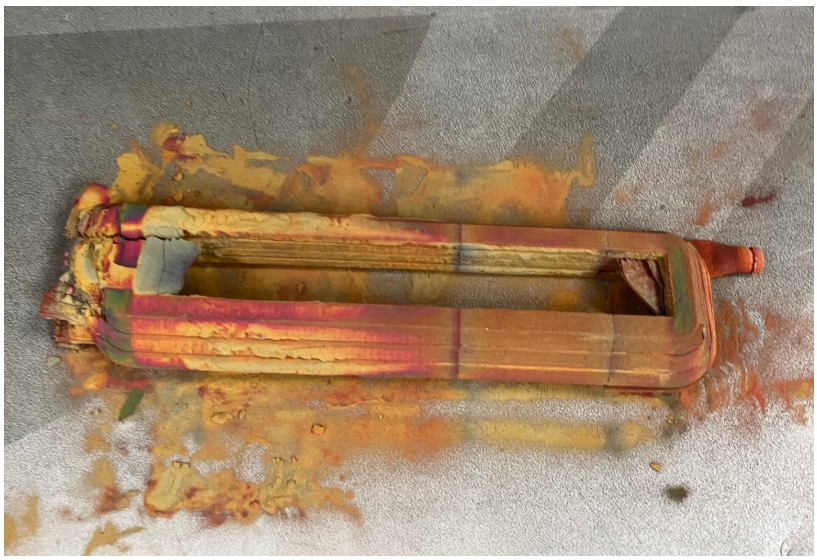

Figure 3.2: Result of the pure copper print.

The fragility of the part is likely due to the limited thickness of the winding's coil walls, particularly in the sections where the channels for the coolant flow are located. In addition to this fragility, despite using a very fine copper powder, once the part was produced, it was impossible to remove the powder from inside the winding's channel. This suggests that the height of the winding channels should be increased.

The component was later treated with shot peening, a surface process designed to enhance fatigue resistance and decrease the risk of fractures. Unfortunately, the winding did not endure this treatment and failed, as shown in Fig. 3.3.

Figure 3.3: Winding printed in copper after shot peening.

3.2 Aluminum printing of the winding

After printing with pure copper, the focus shifted to aluminum printing, using AlSi10Mg powder from EOS. This was done to determine if the structure could endure with a material other than pure copper.

However, this approach also led to the winding failing at the same points as those produced with copper, as illustrated in Fig. 3.4 and Fig. 3.5.

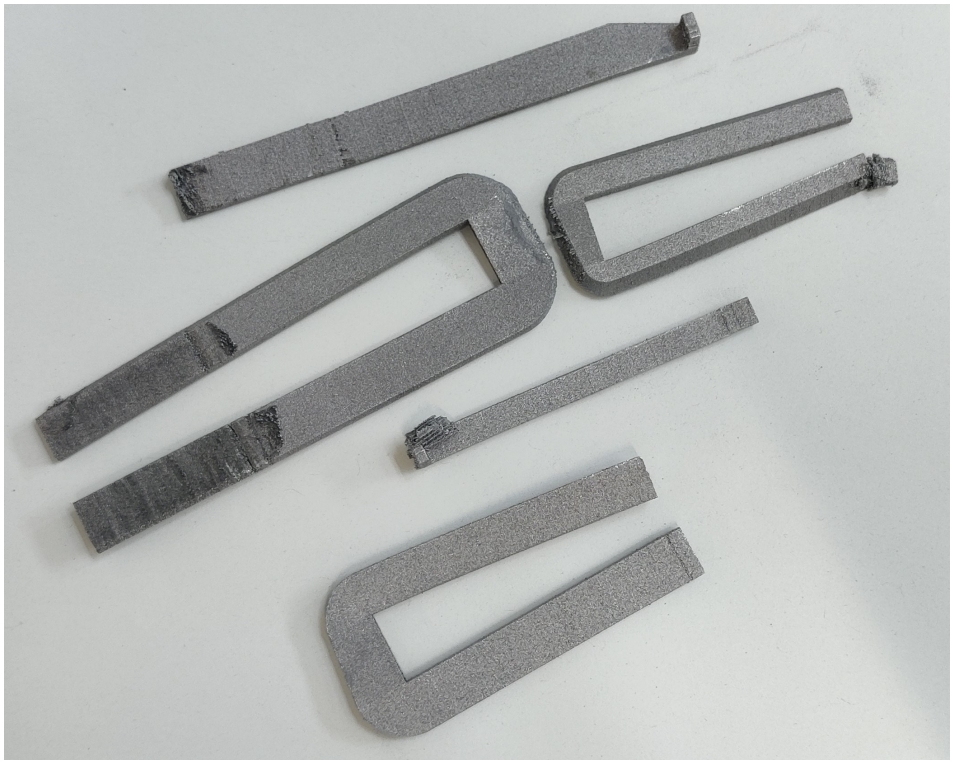

Figure 3.4: Result of the AlSi10Mg print.

This is mainly due to two issues:

1. The winding geometry has excessive constrictions and abrupt changes in shape, which, due to thermal stresses, have caused breakage;
2. during construction, the part goes into resonance, ultimately breaking at a specific point.

The component was built vertically both times to minimize supports, which, even when optimized, can create areas prone to cracking on such thin surfaces. The ratio between the section and height means that each time the 3D printer's

blade spreads the powder, vibrations are generated due to the friction between the molten zone (which has a rough surface) and the blade, inducing micro-oscillations that eventually exceed a limit, leading to breakage. The lower area supporting the part is a replica of the surface and is therefore very small. As a result, it fails to dampen these oscillations and keep the part securely anchored.

Figure 3.5: Result of the AlSi10Mg print part 2.

In Fig. 3.6, the cavities of a section of a winding coil can be observed. The thin wall thicknesses that prevented the structure from holding up are evident. However, it is also noticeable that the elliptical shape of the cavities has not collapsed.

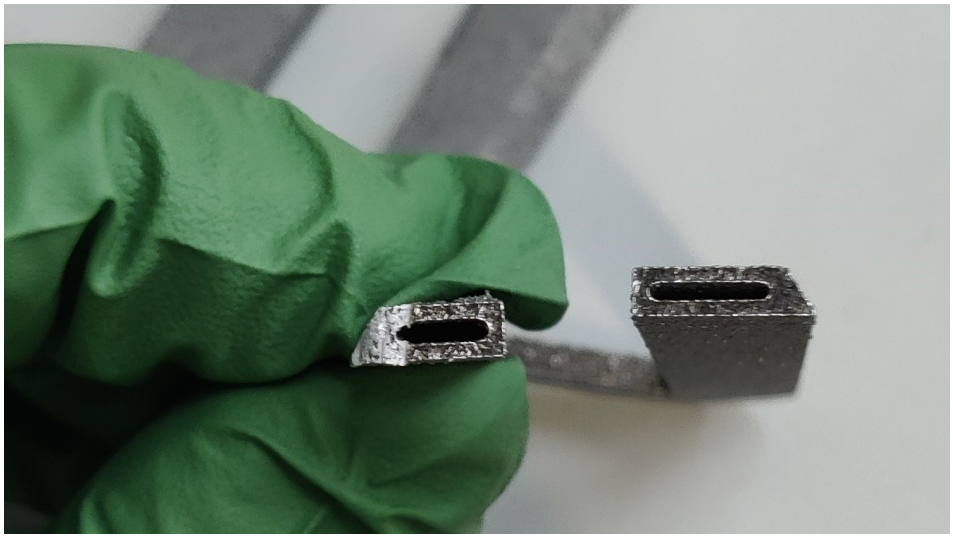

Figure 3.6: Cavities of the section of the AlSi10Mg print.

Chapter 4

Revision of the winding structure

As can be seen from Chapter 3, there are some issues with the winding structure that need to be resolved to ensure the winding is 3D printable and can withstand post-printing treatments. The previously considered winding, sized in Section 2.2, did not fully utilize the entire length of the tooth, as the 3 *mm* (L_LAMINATION) of the tooth near the air gap were not used in order to place the magnetic wedge in that space, a component necessary to reduce losses and thus increase the motor's efficiency.

To improve the physical properties of the winding and ensure it can withstand printing, it is necessary to increase the thickness of the walls of the individual coils and also increase the height of the coil slots. To make these increases, it was decided to fully utilize the tooth by reducing L_LAMINATION from 3 mm to 0.5 *mm*. This way, 2.5 *mm* can be redistributed among the various sections of the winding.

4.1 Sizing of the new winding

Below in Fig. 4.1, the structure of the new winding with the main dimensions is shown.

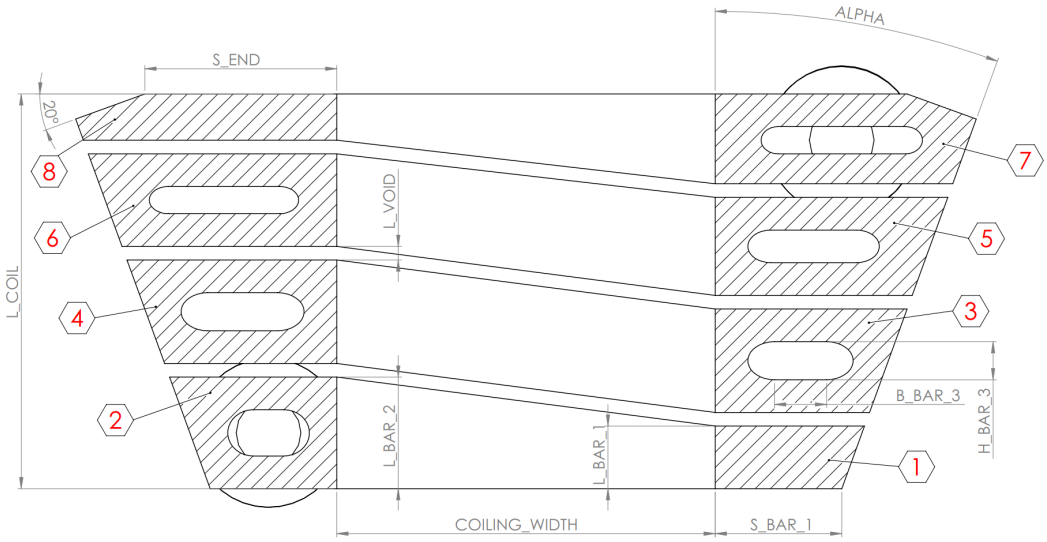

Figure 4.1: Main parameters of the new winding section dimensions.

The following tables present the data of the new winding, in line with the tables previously shown in Section 2.2, to which the reader is referred for a better understanding of the values.

Below, in Table 4.1, the values set by the design are shown.

L_SLOT	15.50	*mm*
L_VOID	0.50	*mm*
L_LAMINATION	0.50	*mm*
L_COIL	14.50	*mm*
L_USEFUL	13.00	*mm*
TOOTH_WIDTH	12.90	*mm*
COILING_WIDTH	13.90	*mm*
S_END	7.05	*mm*
WINDING_DEPTH	102.00	*mm*

Table 4.1: New fixed design values.

The main values of the eight sections of the winding are shown below in Tab. 4.2. It can be observed that the values of L_BAR_i and H_BAR_i have increased compared to those of the previous winding (Tab. 2.3), thanks to the redistribution of the 2.5 *mm*. This increase is important for improving the physical properties of the winding.

Meanwhile, the values of S_BAR_i and B_BAR_i have decreased due to the reduction of the ALPHA angle from 32° to 20°, which was made to allow the

axially grown winding to be inserted into the slot when the adjacent slot is occupied by another winding. This decrease does not negatively affect the physical structure of the winding, as these values were not critical for the printing process.

Dimension	**Value**	**Units**	**Dimension**	**Value**	**Units**
L_BAR_1	2.30	*mm*	**S_BAR_1**	4.65	*mm*
L_BAR_2	4.10	*mm*	**S_BAR_2**	4.65	*mm*
L_BAR_3	3.80	*mm*	**S_BAR_3**	5.67	*mm*
L_BAR_4	3.80	*mm*	**S_BAR_4**	6.32	*mm*
L_BAR_5	3.60	*mm*	**S_BAR_5**	7.23	*mm*
L_BAR_6	3.40	*mm*	**S_BAR_6**	7.89	*mm*
L_BAR_7	3.30	*mm*	**S_BAR_7**	8.73	*mm*
L_BAR_8	1.70	*mm*	**S_BAR_8**	9.31	*mm*
-	**-**	*mm*	**S_END**	7.05	*mm*
Dimension	**Value**	**Units**	**Dimension**	**Value**	**Units**
-	-	*mm*	**-**	-	*mm*
H_BAR_2	1.70	*mm*	**B_BAR_2**	0.98	*mm*
H_BAR_3	1.40	*mm*	**B_BAR_3**	1.91	*mm*
H_BAR_4	1.40	*mm*	**B_BAR_4**	2.56	*mm*
H_BAR_5	1.20	*mm*	**B_BAR_5**	3.15	*mm*
H_BAR_6	1.00	*mm*	**B_BAR_6**	4.09	*mm*
H_BAR_7	1.00	*mm*	**B_BAR_7**	4.53	*mm*
-	**-**	*mm*	**-**	**-**	*mm*
-	**-**	*mm*	**-**	**-**	*mm*

Table 4.2: Main value of the new winding sections.

Below, in Tab. 4.3, the new values of the elliptical slot, obtained from the spreadsheet using the formulas described in Section 2.2, are shown.

Dimension	**Value**	**Units**	**Dimension**	**Value**	**Units**
a_2	0.94	*mm*	**b_2**	0.85	*mm*
a_3	0.98	*mm*	**b_3**	0.70	*mm*
a_4	0.98	*mm*	**b_4**	0.70	*mm*
a_5	0.84	*mm*	**b_5**	0.60	*mm*
a_6	0.70	*mm*	**b_6**	0.50	*mm*
a_7	0.70	*mm*	**b_7**	0.50	*mm*

Table 4.3: Main value of the new groove sections.

In Tab. 4.4, the values of the slot areas for each section of the winding are shown.

Dimension	Value	Units
TUNNEL_AREA_2	4.16	mm^2
TUNNEL_AREA_3	4.83	mm^2
TUNNEL_AREA_4	5.75	mm^2
TUNNEL_AREA_5	5.37	mm^2
TUNNEL_AREA_6	5.19	mm^2
TUNNEL_AREA_7	5.63	mm^2

Table 4.4: Tunnel values in the new sections.

Tab. 4.5 shows the values of the triangle to be "subtracted," as visible in Fig. 2.10.

Dimension	Value	Units
a_{tri}	2.88	mm
b_{tri}	0.98	mm
c_{tri}	2.70	mm
α_{tri}	90	deg
β_{tri}	20	deg
γ_{tri}	70	deg
$Area_{tri}$	1.33	mm^2

Table 4.5: New triangle dimensions.

Tab. 4.6 shows the actual values of the conductive areas of the winding. These values are in line with those of the previous winding (Tab. 2.7).

Dimension	Value	Units
$Area_1$	11.66	mm^2
$Area_2$	17.96	mm^2
$Area_3$	19.34	mm^2
$Area_4$	20.91	mm^2
$Area_5$	23.03	mm^2
$Area_6$	23.74	mm^2
$Area_7$	23.82	mm^2
$Area_8$	15.02	mm^2

Table 4.6: Effective areas of the new conductor sections of the winding.

4.2 Changes made in the new version of the winding

Figures 4.2 and 4.3 show the side views of the two versions of the windings. In particular, it can be observed that in the new version (Fig. 4.3), on the side of the electrical connections, fittings have been constructed to strengthen the structure and prevent stress concentration. These fittings were not included in the first version of the winding because a minimal radius is always achieved during 3D printing due to the construction process. They are added in this new version to enhance the structure and prevent piece failure.

The figures also show that, compared to the first version, the second version features a more gradual increase in the thickness of the hydraulic connection sections (area between the light green dashed lines), leading to greater resistance of these connections.

Figure 4.2: Side view of the first version of the winding.

Figure 4.3: Side view of the modified winding.

From Figures 4.4 and 4.5, the modifications made to the hydraulic connections can be seen more clearly. In particular, in addition to the progressive increase in the thickness of the sections, the fittings have been enlarged to better support the weight of the connections, as the attachment points between the hydraulic connections and the winding coils were found to be critical in the first version.

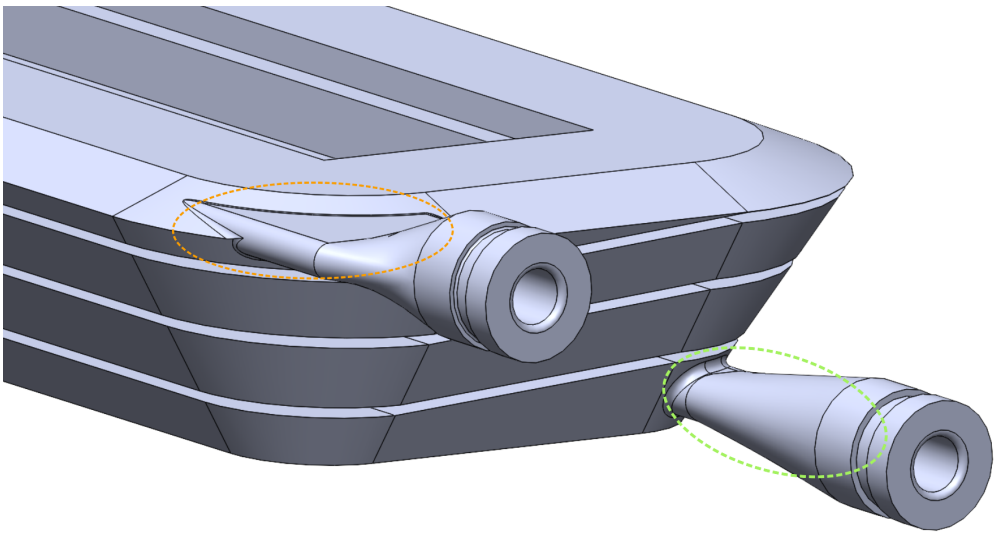

Figure 4.4: View of the hydraulic connections of the first version of the winding.

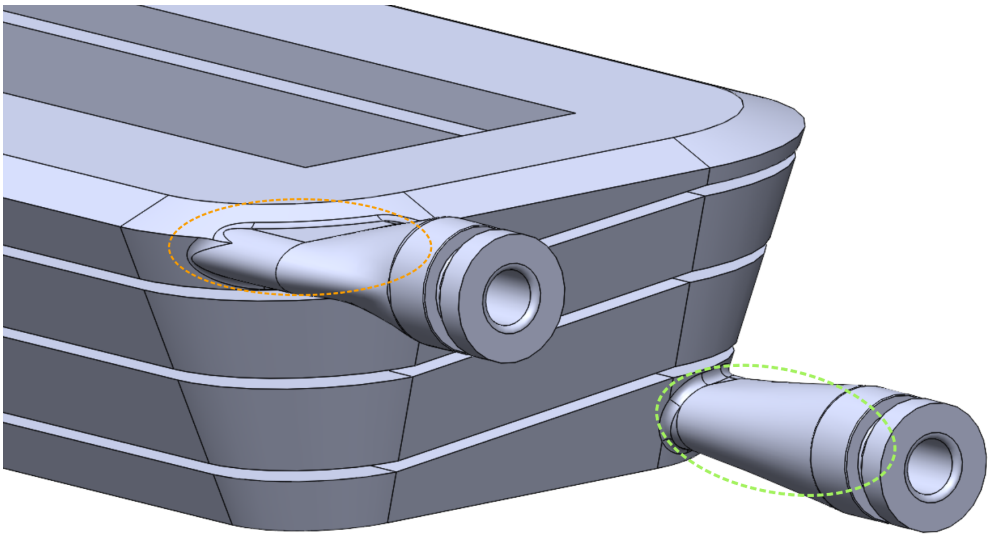

Figure 4.5: View of the hydraulic connections of the modified version of the winding.

From Figures 4.6 and 4.7, the increase of 2.5 *mm* in the axial length of the winding can be observed. These 2.5 *mm* have been redistributed across the various sections to increase the wall thicknesses and the slot heights, in order to achieve a more robust structure and to prevent metal powder from being trapped inside the slots after the piece is printed.

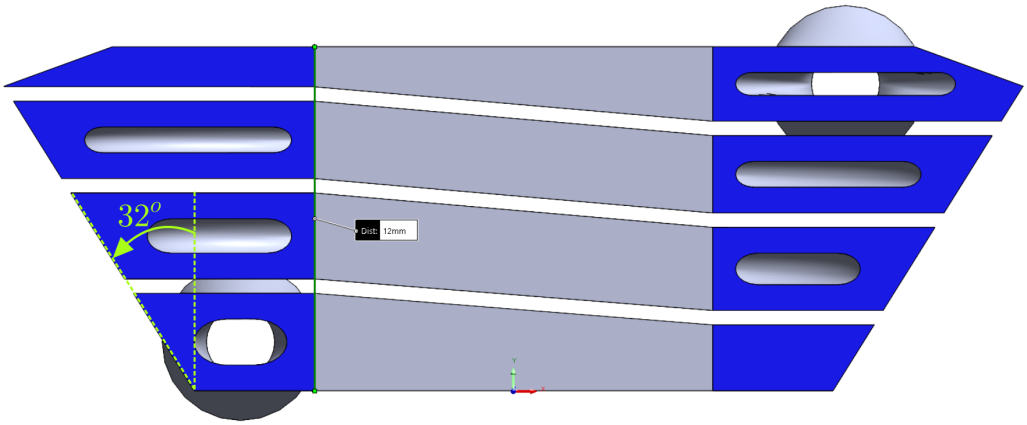

Figure 4.6: Section view of the first version of the winding.

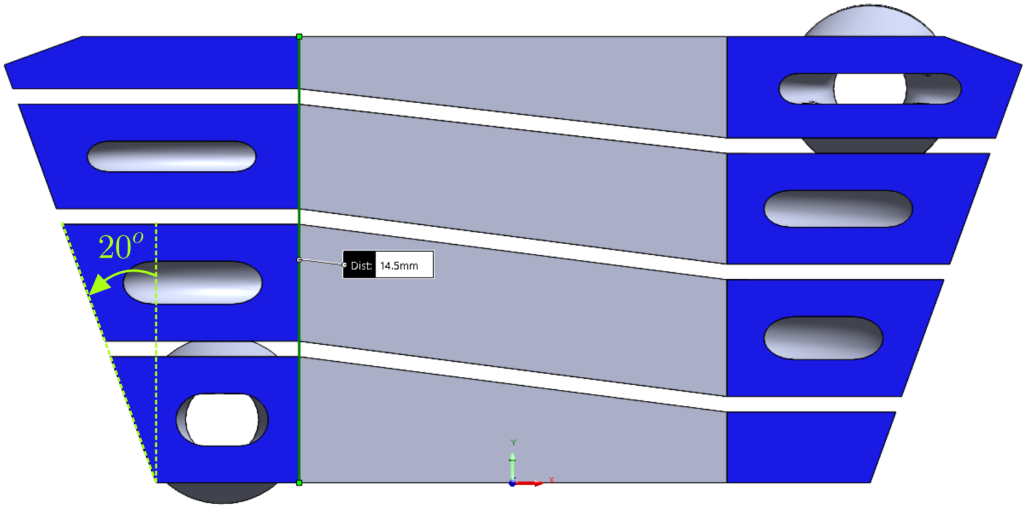

Figure 4.7: Section view of the modified version of the winding.

From Figures 4.8 and 4.9, it can be seen that the minimum wall thickness of the winding sections has increased from 0.9 *mm* to 1.2 *mm*, achieved through the redistribution of the 2.5 *mm* gained in the new configuration. This increase in thicknesses is expected to enhance the winding's resistance during construction and improve its resistance to the pressure of the refrigerant fluid flowing through it.

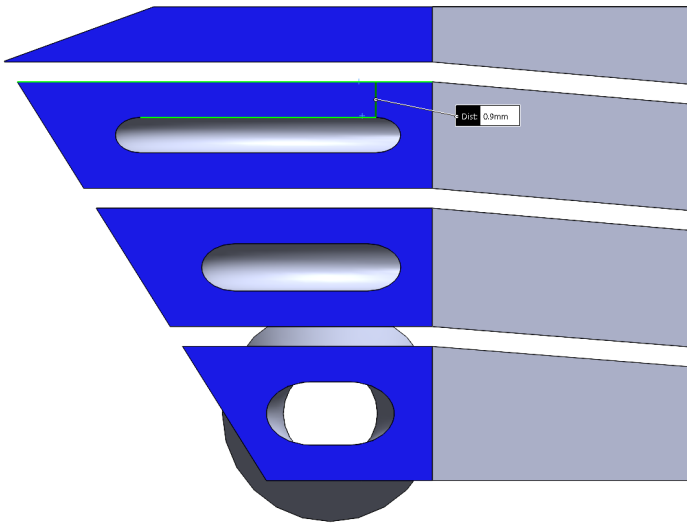

Figure 4.8: View of the wall thickness of the first version of the winding.

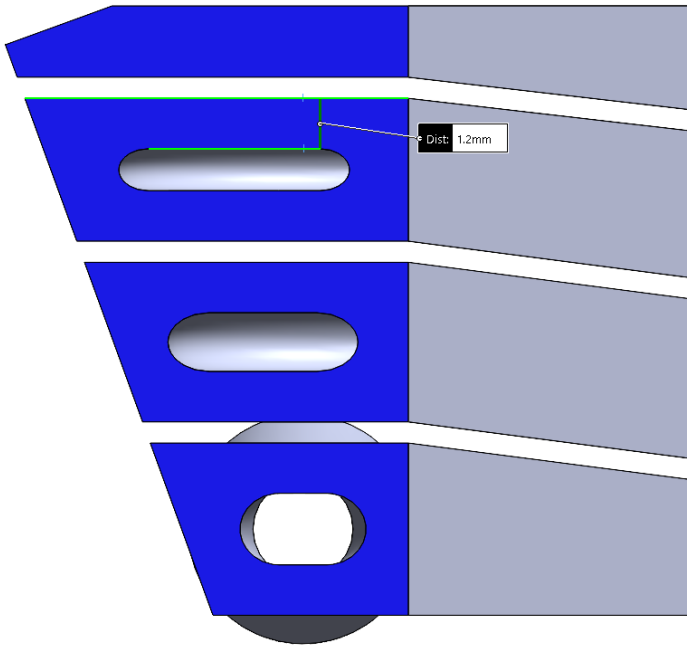

Figure 4.9: View of the wall thickness of the modified version of the winding.

Finally, from Figures 4.10 and 4.11, it can be seen that the minimum slot height of the winding has increased from 0.8 mm to 1.0 mm, also thanks to the redistribution of the 2.5 mm. The increase in slot height not only enhances the resistance of the slot itself but should also allow metal powder to exit more easily after the winding is printed, as the slot section is larger and the risk of unintended welding between the slot walls is reduced.

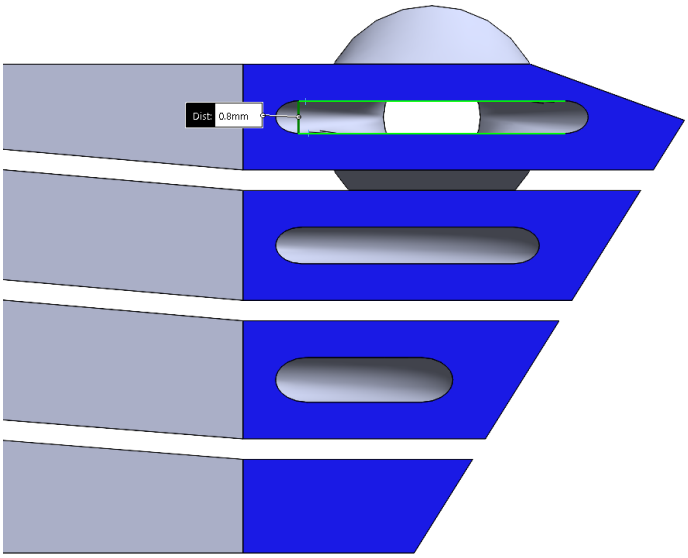

Figure 4.10: View of the slot height of the first version of the winding.

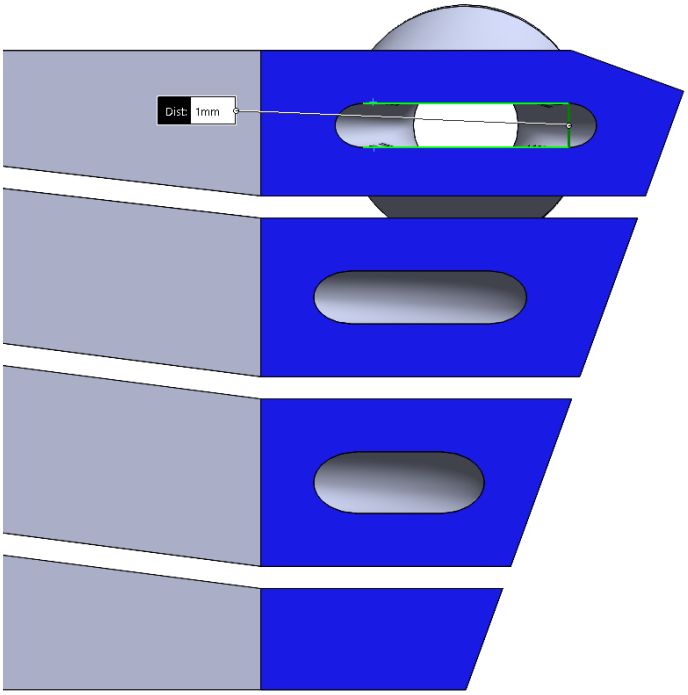

Figure 4.11: View of the slot height of the modified version of the winding.

4.2.1 The motor with the new winding configuration

Having modified the winding structure, it was obviously necessary to also modify the structure of the coolant fluid manifold. Thanks to the increased height of the winding, it was also possible to increase the thickness between the two chambers inside the coolant fluid manifold. Moreover, the two ends connected to the pump were offset compared to the previous case to allow for a better coupling with the pump. In Fig. 4.12, the new views of the motor configuration with the second version of the winding can be seen.

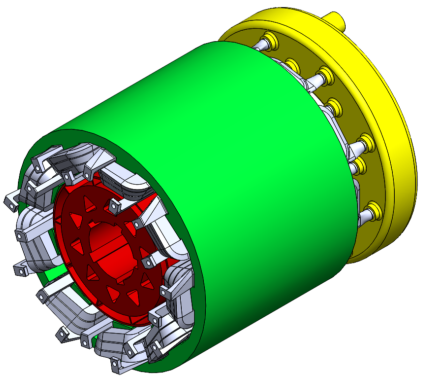

(a) Isometric view of the electrical side

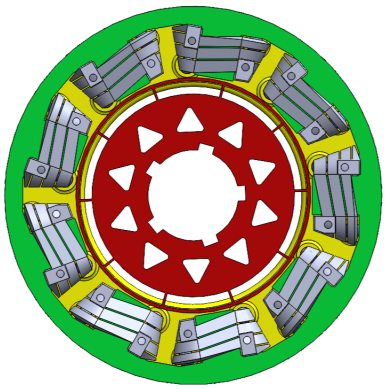

(b) Front view of the electrical side

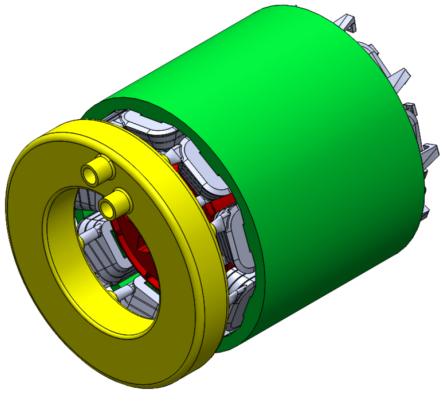

(c) Isometric view of the hydraulic side

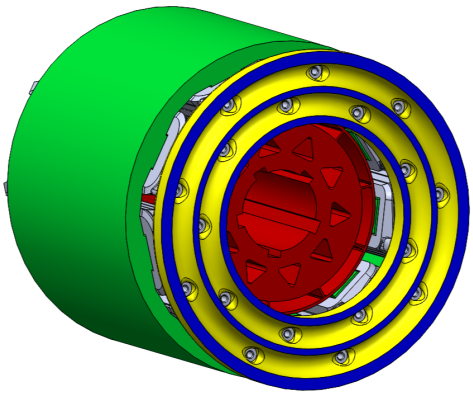

(d) View with the manifold sectioned

Figure 4.12: Views of the motor with the new winding configuration.

4.3 Printing of the new configuration

The second configuration of the winding was then printed using the same printer as the first version and was made from AlSi10Mg. The printing process lasted approximately 9 hours, after which the winding was allowed to cool slowly inside the printer overnight. Once removed from the printer and after the excess metal powder was cleaned off, the winding appeared as shown in Fig. 4.13.

(a) Electrical side view

(b) Hydraulic side view

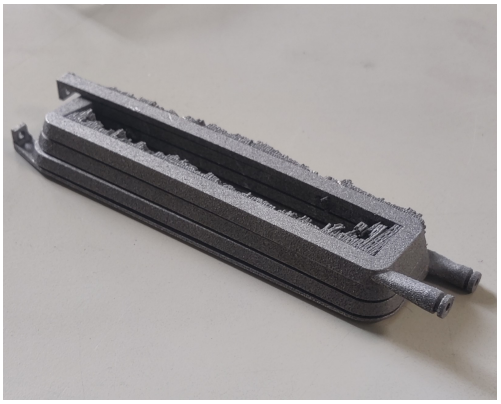

(c) View from below

(d) Top view

Figure 4.13: Views of the winding after printing.

It is possible to notice the presence of the supports that were built during the printing process to allow the structure of the winding to sustain itself. In particular, unlike the two prints described in Chapter 3, this print was not made with the piece positioned vertically but rather by constructing the piece placed horizontally with a slight tilt. This was done to increase the support

width relative to the height, thus avoiding the problems encountered in the prints of the first winding configuration. Thanks to this arrangement, the piece does not resonate, and the vibrations are absorbed by a larger support base.

These supports, not being part of the original geometry, must be removed. Usually, a special chisel and hammering are used to remove the bulkier part of the supports, while the supports closer to the surface are removed with pliers, as shown in Fig. 4.14. This method, being more delicate, helps avoid breaking the piece, which, when freshly printed, has internal stresses and a certain fragility. In fact, once the supports are removed, the piece must undergo treatments such as stress-relieving and shot peening.

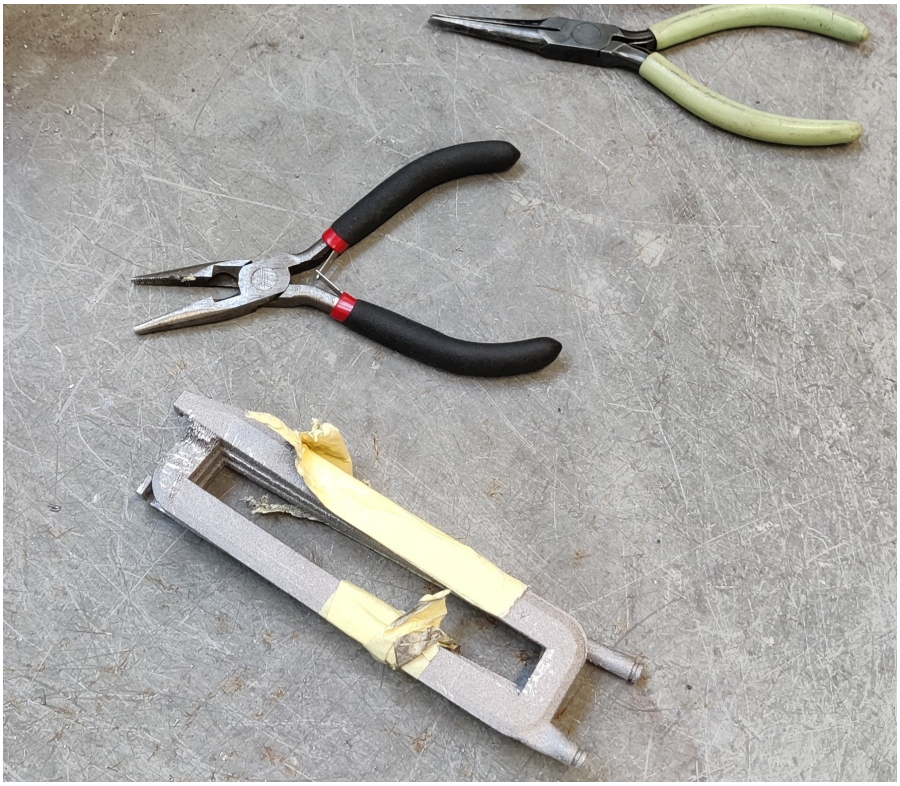

Figure 4.14: Winding and clamps during supports removal.

In Fig. 4.15, it is possible to see how the piece looks once the bulkier parts of the supports have been removed. In particular, the base structure of the supports can be observed, which exhibits a certain honeycomb pattern. The removal of these remaining parts does not significantly affect the final structure of the winding, as they are designed to be easily removed.

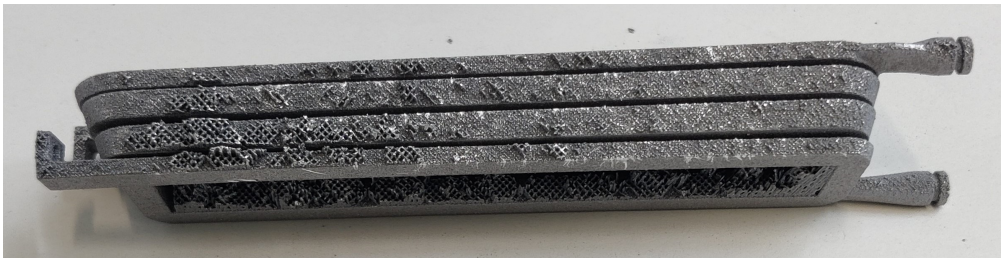

Figure 4.15: Base structure of the supports.

Finally, after removing all the supports and sanding the various parts with sandpaper, the winding appears as shown in Fig. 4.16. It is particularly noticeable that the structure is not perfectly aligned but exhibits some curvatures due to the internal stresses developed during the 3D printing process. Additionally, it can be seen that in Fig. 4.13 these curvatures were not present because the supports held the structure firmly.

(a) Isometric view of the electrical side

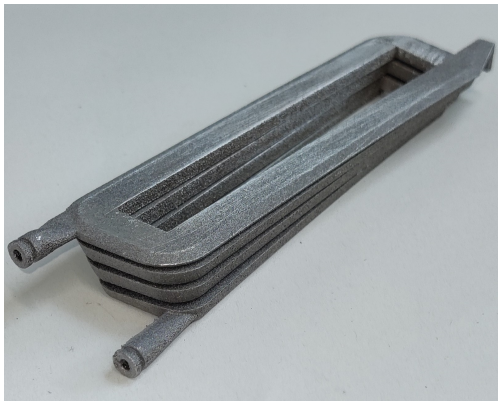

(b) Isometric view of the hydraulic side

(c) Front view of the electrical side

(d) Front view of the hydraulic side

Figure 4.16: Views of the winding after support removal.

Chapter 5

Multiphysics simulations of winding through COMSOL

COMSOL Multiphysics is an advanced simulation software that allows for the modeling and analysis of complex physical phenomena. Its strength lies in its ability to handle multiphysics problems, where multiple physical phenomena interact with each other, such as heat transfer, fluid dynamics, electromagnetism, and structural mechanics. The software offers a wide range of specialized modules for disciplines like electromagnetism, acoustics, and structural engineering, enabling precise simulations in various industrial sectors.

One of COMSOL's most powerful features is its ability to manage coupled simulations, where variables from one domain directly influence other physical phenomena. This capability is essential for the design of advanced products and the study of complex processes that involve the interaction of multiple physical fields. The software is compatible with other CAD modeling tools and can interface with MATLAB for more in-depth analysis. Additionally, COMSOL provides advanced tools for mesh creation, numerical solving, and post-processing, allowing users to visualize results in a detailed and intuitive manner through graphs and three-dimensional maps.

In this thesis work, COMSOL was used to simulate the behavior of the winding under its operating conditions within the motor. For this reason, various coupled physics were analyzed to obtain results that are as accurate and realistic as possible. Specifically, the physics used were:

- *Magnetic Fields*;
- *Laminar Flow*;

- *Heat Transfer in Solids.*

Thanks to COMSOL's capability to analyze these physics with their respective interactions, the results, presented later in this chapter, accurately replicate the real behavior of the winding.

5.1 Definition of the physics and model parameters

Below is a brief explanation of how the winding simulation was set up in COMSOL.

Starting with the Select Space Dimension, the *3D* option was chosen. Then, the physics were selected following these paths:

- *AC/DC* → *Electromagnetic Fields* → *Magnetic Fields*;
- *Fluid Flow* → *Single-Phase Flow*→ *Laminar Flow*;
- *Heat Transfer* → *Heat Transfer in Solids.*

Next, the type of study was chosen, and in this case, *Empty Study* was selected. The main features of the study were then defined, and the COMSOL interface appeared on the screen.

5.1.1 Geometry

Next, the geometry of the element to be analyzed, in this case, the winding, was defined. Specifically, the geometry of the winding, developed using SolidWorks, was imported using the *CAD Import Module*, after previously setting the length unit of the study to mm. Subsequently, in the *Parameters* section, the frequency at which the winding will operate was defined, i.e., $f = 1500Hz$

Then, following the path *Definitions* → *Selections* → *Explicit*, various domains and boundaries present in the winding were defined for convenience. Specifically, the following were defined:

- Coil;
- Water & Glycol;

- Coil + Water and glycol;
- Resin;
- Coil surface.

5.1.2 Materials

The definition of the various materials was then carried out. In particular, the Water + Glycol solution was selected from the COMSOL material library, with its main parameters listed in Tab. 5.1. This solution was assigned to the previously defined domain, Water & Glycol, as shown in Fig. 5.1.

Property	**Value**	**Unit**
Dynamic viscosity	eta(T)	$Pa \cdot s$
Heat capacity at constant pressure	Cp(T)	$J/(kg \cdot K)$
Density	rho(T)	kg/m^3
Thermal conductivity	k(T)	$W/(m \cdot K)$
Relative permeability	1	-
Relative permittivity	80	-
Electrical conductivity	1	S/m

Table 5.1: Main properties of Water and Glycol.

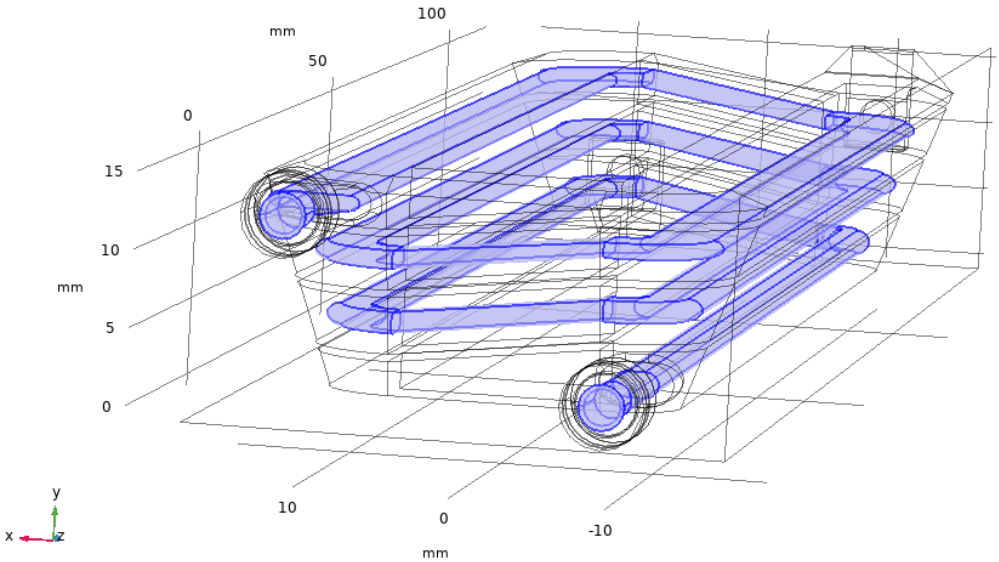

Figure 5.1: Water & Glycol domain.

For the winding, the material AlSi10Mg was created using the properties defined in the datasheet[1] of the metallic powder used during the prototype printing phase. The main properties are listed in Tab. 5.2, and Fig. 5.2 shows the view of the domain where AlSi10Mg is applied in the as-built condition.

Property	**Value**	**Unit**
Heat capacity at constant pressure	900	$J/(kg \cdot K)$
Density	2670	kg/m^3
Thermal conductivity	105	$W/(m \cdot K)$
Relative permeability	1	-
Relative permittivity	1	-
Electrical conductivity	$1.450 \cdot 10^7$	S/m

Table 5.2: Main properties of AlSi10Mg in the as-built condition.

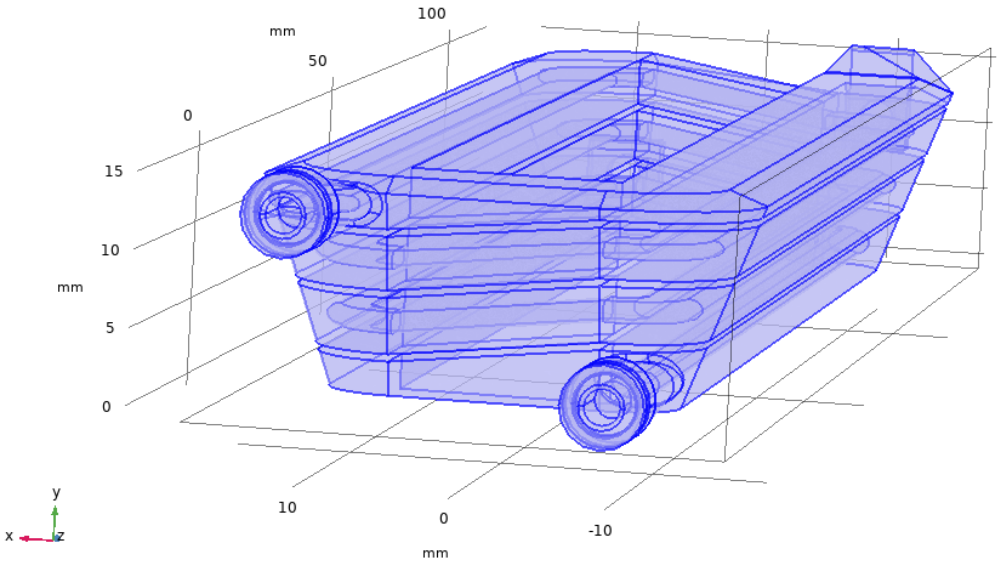

Figure 5.2: AlSi10Mg domain [4].

Finally, considering that the winding, once housed within the stator slot, will be covered with resin both to insulate each turn from the others and to isolate the winding from the stator, a material was created in COMSOL using the properties derived from the manufacturer's datasheet. In particular, a resin *Elan-tron MC62/W363*[2] with excellent thermal conductivity was chosen

[1] EOS Aluminium AlSi10Mg
[2] ELANTAS website

to facilitate efficient heat removal. The main properties of this resin are listed in Tab. 5.3, and Fig. 5.3 shows the domain where it was defined, taking into account the space within the stator slot.

Property	**Value**	**Unit**
Heat capacity at constant pressure	1900	$J/(kg \cdot K)$
Density	1620	kg/m^3
Thermal conductivity	0.90	$W/(m \cdot K)$
Coefficient of thermal expansion	$125 \cdot 10^{-6}$	$1/K$
Relative permittivity	2.3	-

Table 5.3: Main properties of Elan-tron MC62/W363 [11].

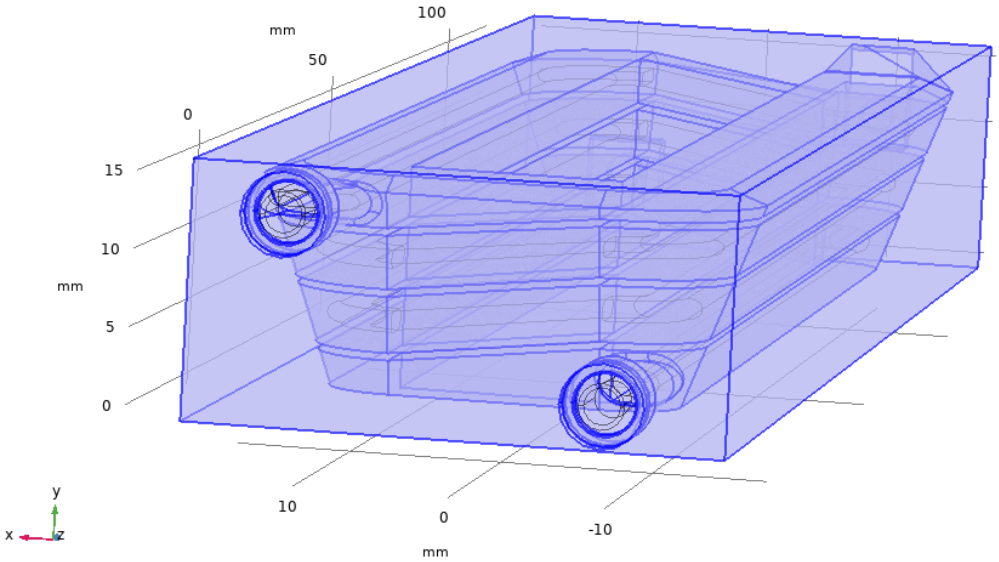

Figure 5.3: Elan-tron MC62/W363 domain.

5.1.3 Physics

Magnetic Fields

Starting from the first physics involved, which is *Magnetic Fields*, the *Coil* function is introduced, allowing for a more detailed study of the winding. From this section, the excitation of the winding can be defined; in this simulation, a current of 200 A was chosen, which corresponds to the one required for the motor described in Section 2.1. This physics was applied only to the Coil domain. The input, corresponding to the point where the winding is powered, and the output, corresponding to the point where the star center of the three-phase set is closed, were also selected. Specifically, the upper terminal of the winding (section 8) was chosen as the input, and the lower terminal (section 1) was chosen as the output.

Laminar Flow

To model the behavior of the cooling fluid inside the winding, the *Laminar Flow* physics was chosen and applied to the Water & Glycol domain. The fluid properties are directly retrieved from the materials, leaving only the definition of inlet and outlet conditions for the internal conduit of the winding. Specifically, a mass flow rate of $1.4 \cdot 10^{-3} kg/s$ was chosen as the input, and the lower conduit (section 2) was selected since it has a shape closer to a circular section. For the outlet, a pressure condition of 0 Pa was imposed, considering a reference pressure of 1 atm, and the upper conduit (section 7) was selected.

Heat Transfer in Solids

The modeling of heat exchange between the winding, the cooling fluid, and the resin was carried out using the *Heat Transfer in Solids* physics, which was applied to all defined domains. The material properties are automatically included in the physics. The initial temperature of the system was set to $20°C$, and the inlet temperature of the cooling fluid was also set to $20°C$. The heat source was imposed using the function *withsol('sol1',mf.Qh)*, through which the heat losses calculated in solution 1, i.e., the solution where the electrical problem is analyzed, are incorporated into this physics.

5.1.4 Mesh

Before proceeding with the multiphysics study of the problem, it is necessary to generate a *Mesh*. The mesh can be automatically generated by COMSOL, but in this case, it was manually generated to achieve greater precision, particularly inside the cooling fluid channels and electrical terminals. Specifically, a *Free Triangular* mesh was used for the electrical terminals and hydraulic connections, while a *Free Tetrahedral* mesh was used for the remaining geometry. Figures 5.4 and 5.5 show the mesh[3] with a view of the electrical side and the hydraulic side, respectively.

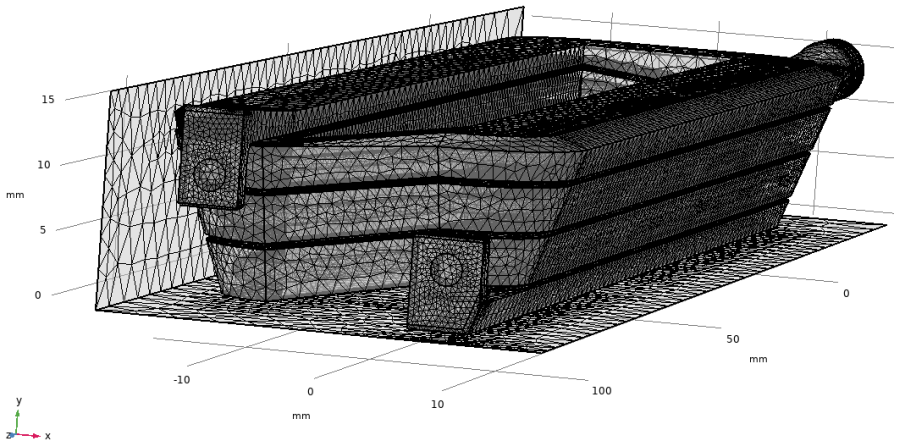

Figure 5.4: Electrical side mesh.

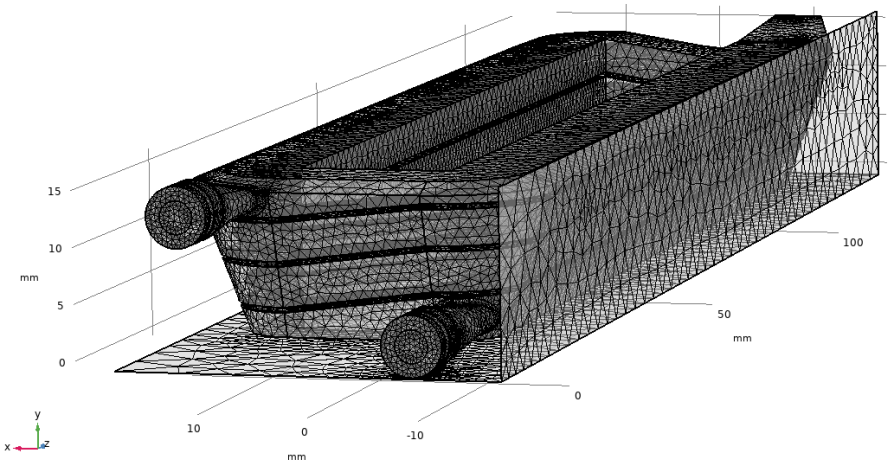

Figure 5.5: Hydraulic side mesh.

[3]It is specified that in the figures, some sides of the resin domain have been hidden to allow for better visualization of the overall structure.

5.1.5 Studies

Finally, the actual study of the selected physics is undertaken. Specifically, two studies are conducted: the first addresses the electrical problem, and the second focuses on solving the fluid dynamics and thermal problems.

Study 1

This first study is conducted in two steps:

- *Coil Geometry Analysis*, which allows for the study of a winding;
- *Frequency Domain*, which enables frequency analysis, and in this study, a frequency of 1500 Hz was selected.

These two steps focus on the Magnetic Fields physics.

Study 2

With the results obtained from Study 1, a *Stationary* step is performed where the *Laminar Flow* and *Heat Transfer in Solids* physics are solved. This study will then allow for the quantitative analysis of various properties, such as the winding temperature, the coolant temperature, the resin temperature, the winding resistance, the fluid pressure, the fluid velocity, and so on.

5.2 Results of the multiphysics simulation

The following paragraph presents the results of three different simulations in order to highlight the differences. In particular, the three simulations are:

1. the winding in the as-built condition;
2. the winding after undergoing heat treatment;
3. the winding after undergoing heat treatment with a higher flow rate.

For each of these cases, the results include:

- temperature distribution;
- current density;
- cooling fluid velocity;
- pressure variation.

5.2.1 Simulation with the as-built winding

In this simulation, the winding was analyzed just after coming out of the 3D printer, thus in the as-built condition. In this condition, AlSi10Mg, according to the EOS catalog, has a conductivity of 25% IACS, which corresponds to an electrical conductivity of $c = 1.450 \cdot 10^7\, S/m$. Therefore, it is lower than what would be obtained after a heat treatment. As previously described, the simulations were conducted at $f = 1500\, Hz$ and at the maximum operating current of 200 A. From the COMSOL simulation, a power loss of $P_{losses} = 83.654\, W$ is obtained.

From Fig. 5.7, the temperature distribution obtained in the simulation can be observed, highlighting the temperatures reached by the cooling fluid, the winding, and the resin. It can be noted that the temperature is higher in the area of the electrical terminals and in sections 1 and 8, which are those without channels for the cooling fluid passage. Specifically, a maximum temperature of $66°C$ is recorded, while the minimum corresponds to the inlet temperature of the cooling liquid, which is $20°C$.

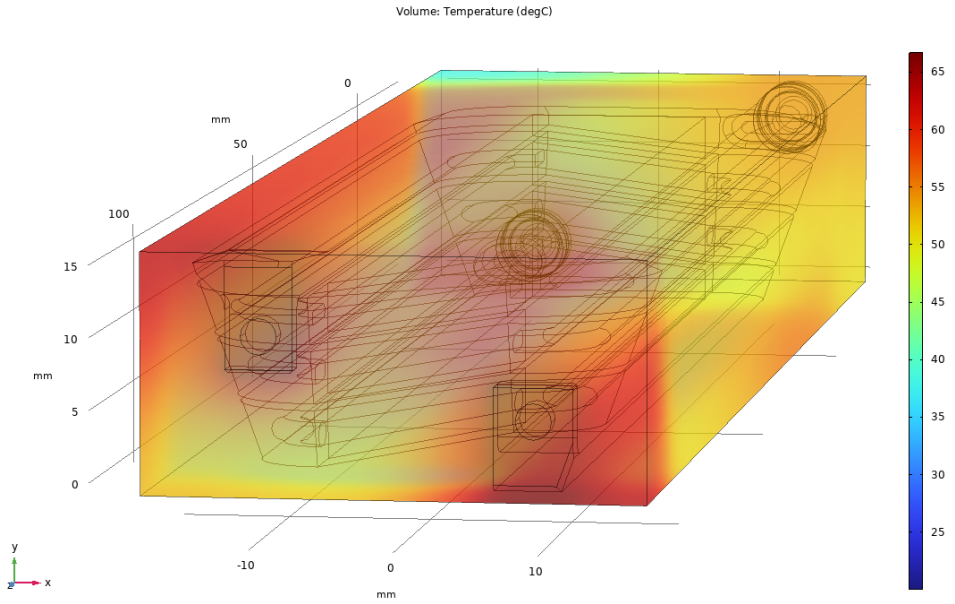

Figure 5.6: Temperature of the winding, cooling fluid, and resin in the as-built condition.

In Fig. 5.7, the same temperature distribution result analyzed in the previous figure is shown, but the resin domain has been hidden to make the temperature distribution on the winding more appreciable.

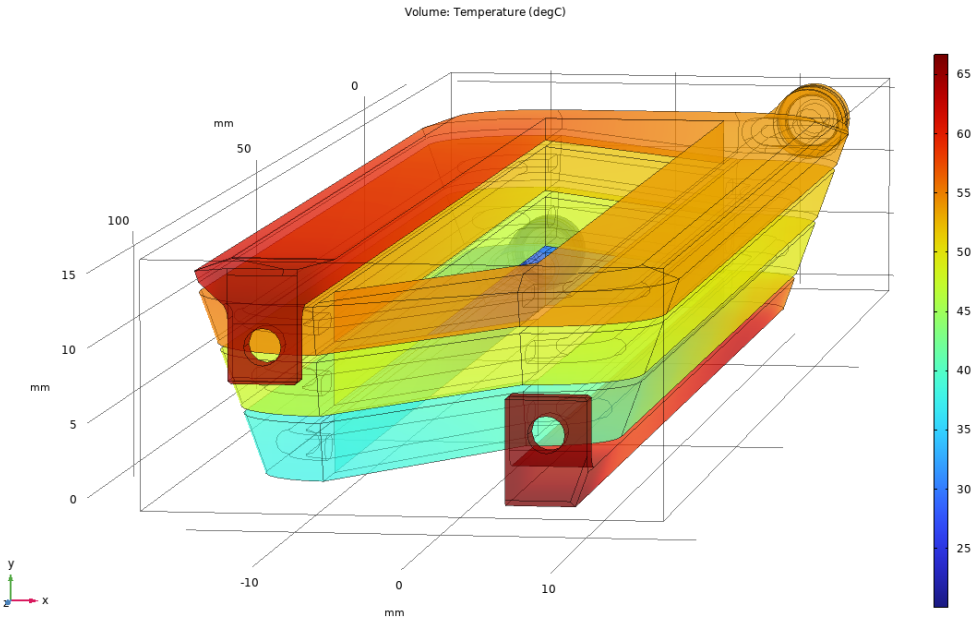

Figure 5.7: Temperature of the winding and cooling fluid in the as-built condition.

In particular, it can be observed that the lowest temperature is reached on the hydraulic side (section 2), where the cooling fluid enters at a temperature of 20°C. The highest temperature is recorded, besides in the sections without cooling fluid channels, at the electrical terminals. In this simulation, the conduction between the electrical terminals, the power supply, and the star center closure was not considered, so in reality, a lower temperature is expected, as the heat would have a path for dissipation.

In Fig. 5.8, the current density in various points of the winding can be seen. Specifically, it can be observed that most of the winding has a current density between 5 and 10 A/mm^2. The sections with higher current density are those without the cooling fluid channels, namely sections 1 and 8 (described in Fig. 4.1). This is due to the fact that these two sections have the smallest areas, as shown in Table 4.6. In particular, section 8 reaches a current density of about 15 A/mm^2, and section 1 exceeds 20 A/mm^2.

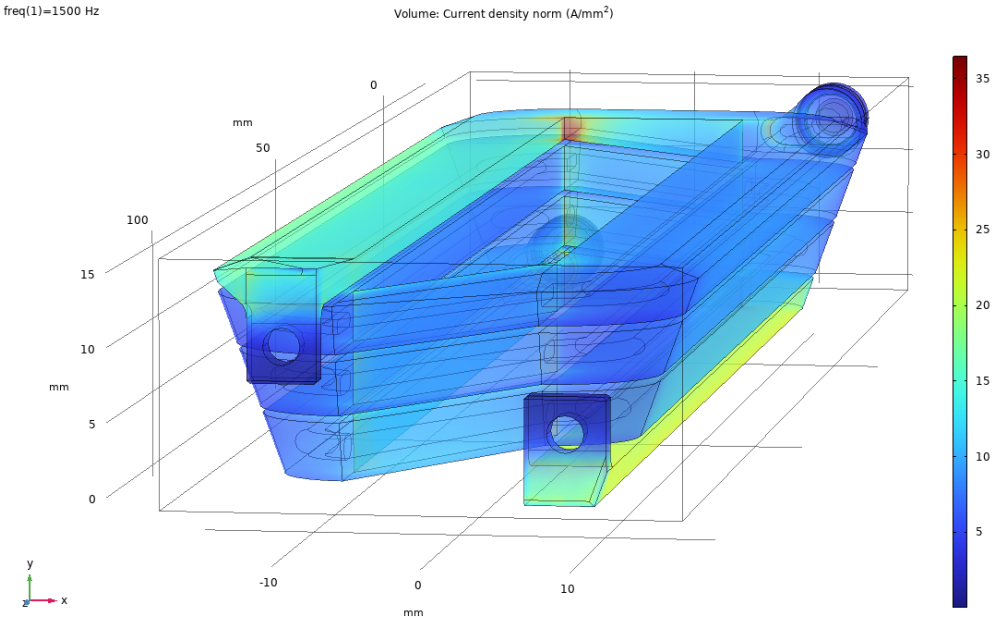

Figure 5.8: Current density in the as-built condition.

Fig. 5.9 shows the velocity profile of the cooling fluid. In addition to the main view, slices have been added to provide a better view of the velocities in various sections inside the channel. As expected, it can be observed that the velocity is higher in the center of the channel section and approaches zero as it nears the channel walls. This is true everywhere except in section 7, which

corresponds to the section with the largest channel area, as described in Tab. 4.4.

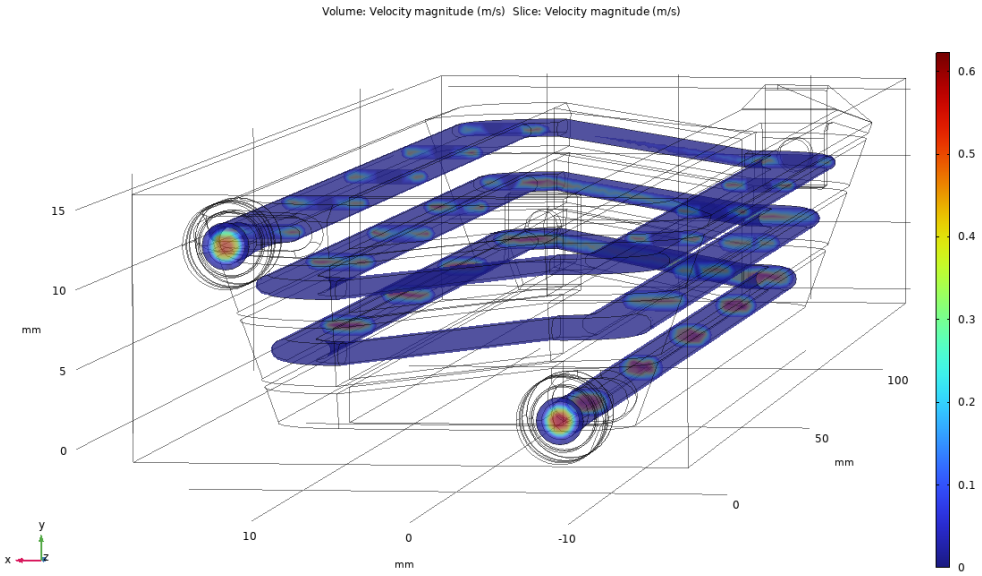

Figure 5.9: Cooling fluid velocity in the as-built condition.

In Fig. 5.10, the pressure profile inside the cooling fluid channel can be observed. Specifically, a pressure drop of about 250 *mbar* can be noted between the inlet and the outlet.

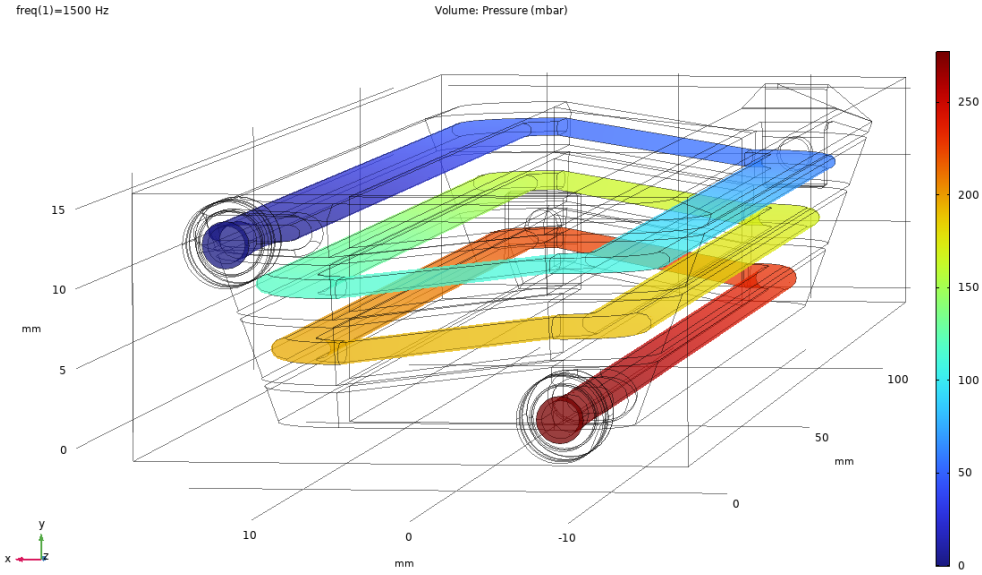

Figure 5.10: Pressure trend in the as-built condition.

5.2.2 Simulation with the winding after heat treatment

In this simulation, the winding is analyzed after undergoing the stress-relieving heat treatment (HT). In this condition, thanks to the heat treatment, the electrical conductivity has increased compared to the previous case. Specifically, from the measurements on the winding described in Paragraph 6.2, after the heat treatment, the electrical conductivity of AlSi10Mg is 40.7% IACS, which corresponds to $c = 2.356 \cdot 10^7\, S/m$. Additionally, the thermal conductivity has also increased, according to the EOS datasheet, rising from 105 $W/(m \cdot K)$ to 160 $W/(m \cdot K)$. These values must be updated in Tab. 5.2.

As previously described, the simulations were conducted at $f = 1500\, Hz$ and at the maximum operating current of 200 A. From the COMSOL simulation, a power loss of $P_{losses} = 57.332\, W$ is obtained, which is noticeably lower than in the previous (as-built) case, thanks to the increased conductivity and consequently the reduced resistance.

In Fig. 5.11, it can be observed that, having kept all conditions identical to the previous case and only modifying the electrical and thermal conductivity of AlSi10Mg, the average temperature is lower compared to the previous case shown in Fig. 5.6. Specifically, the maximum temperature is about $50°C$.

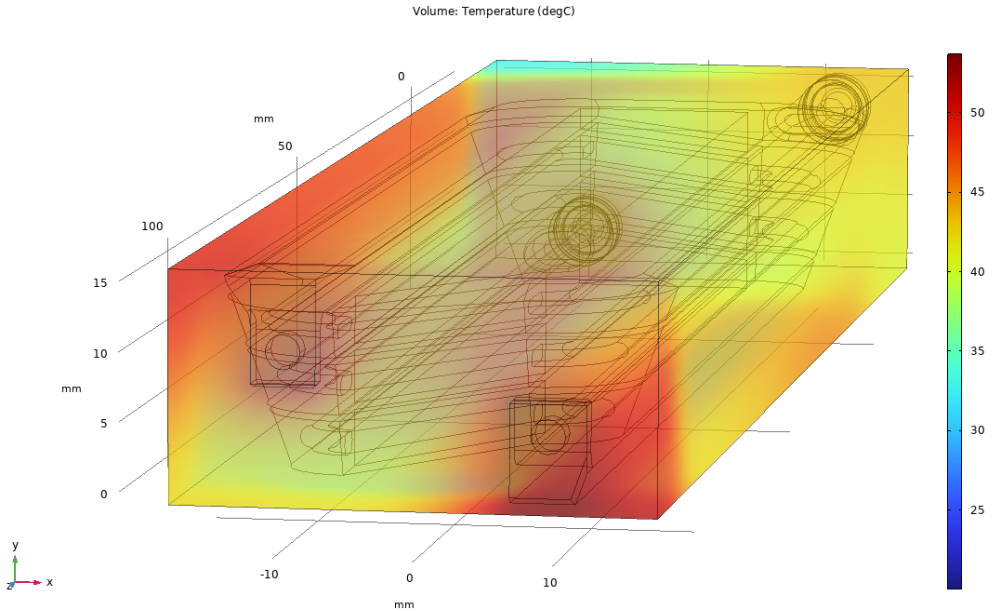

Figure 5.11: Temperature of the winding, cooling fluid, and resin after HT.

In Fig. 5.12, as in the previous simulation, the temperature distribution of

the winding and the cooling liquid is shown, with the temperature distribution in the resin hidden. Essentially, the temperature distribution is the same as in the previous case, but with lower values. The highest temperature is still obtained at the electrical terminals, as previously described.

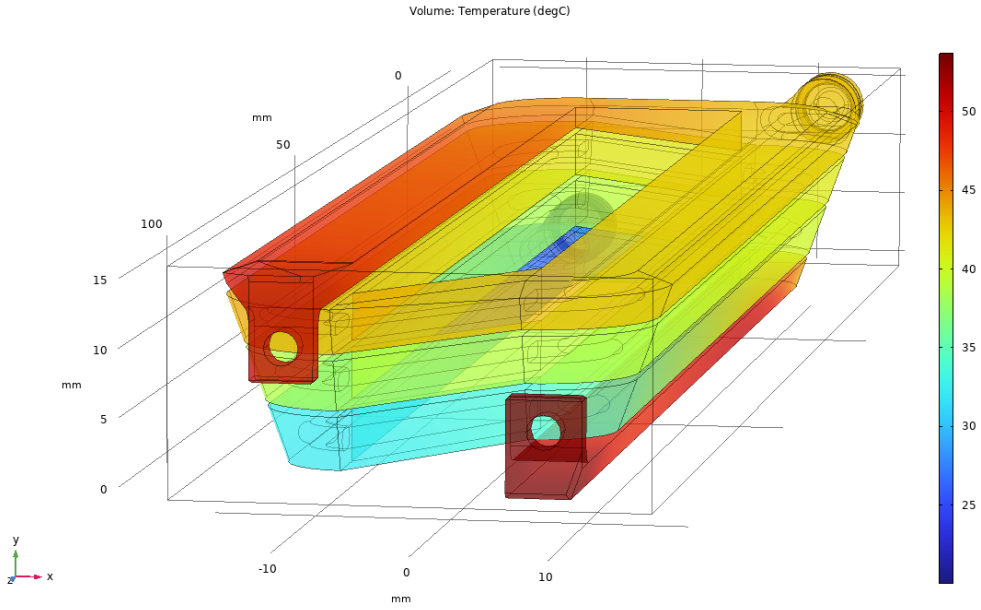

Figure 5.12: Temperature of the winding and cooling fluid after HT.

In Fig. 5.13, the current density in the winding is shown.

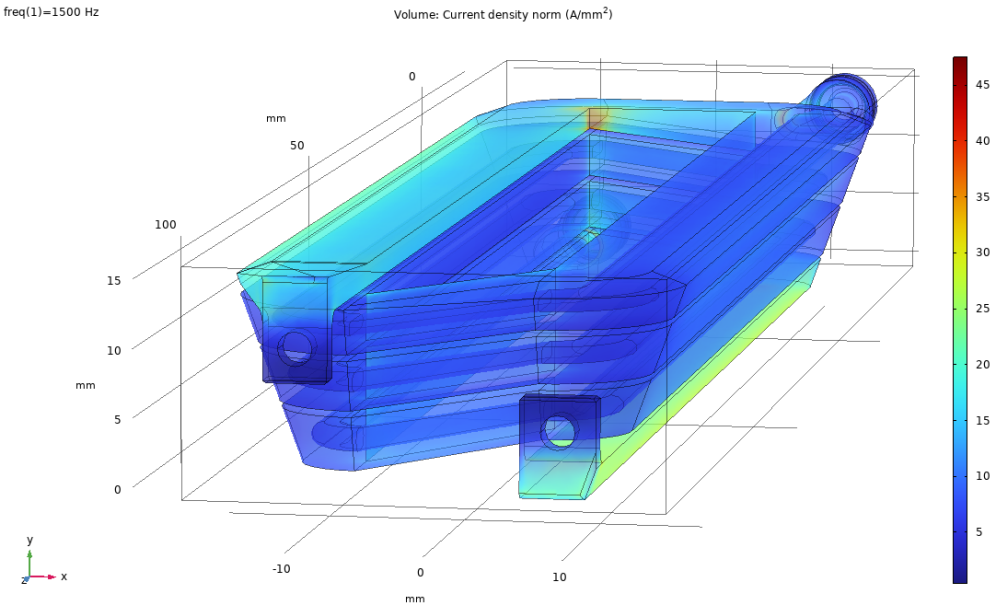

Figure 5.13: Current density after HT.

It can be observed that compared to the previous case, there is a slight increase in the current density in the various sections of the winding.

From Fig. 5.14 and Fig. 5.15, it can be observed that the fluid velocity profile is identical to that of the previous case, while the pressure variation has slightly increased.

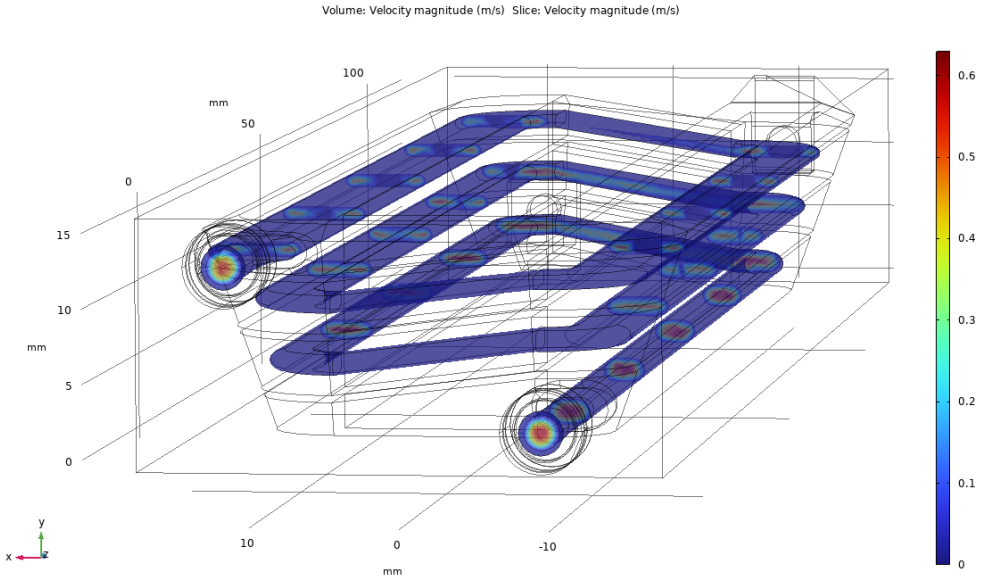

Figure 5.14: Cooling fluid velocity after HT.

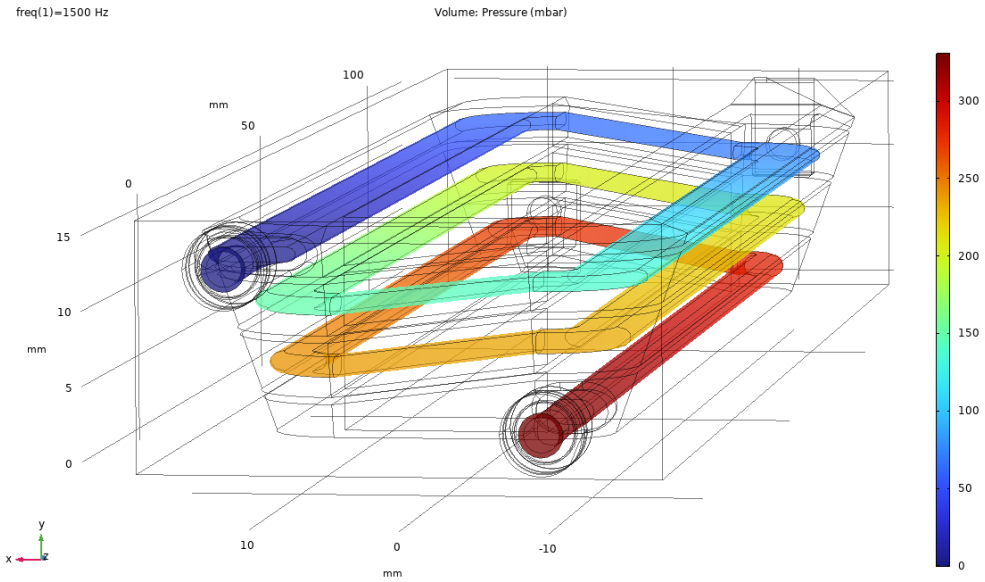

Figure 5.15: Pressure trend after HT.

5.2.3 Simulation with the winding after heat treatment with higher flow rate

In this simulation, the winding (still after heat treatment) is subjected to a higher flow rate (HFR) compared to the previous case in order to analyze the differences between the two cases. Specifically, the refrigerant liquid flow rate used in this simulation is 0.0020 kg/s.

In Fig. 5.16, it can be observed that the temperature distribution, particularly the maximum temperature reached by the resin and the winding, is approximately 5°C lower compared to the previous case. This is due to the higher refrigerant fluid flow rate, which allows for greater heat extraction from the winding.

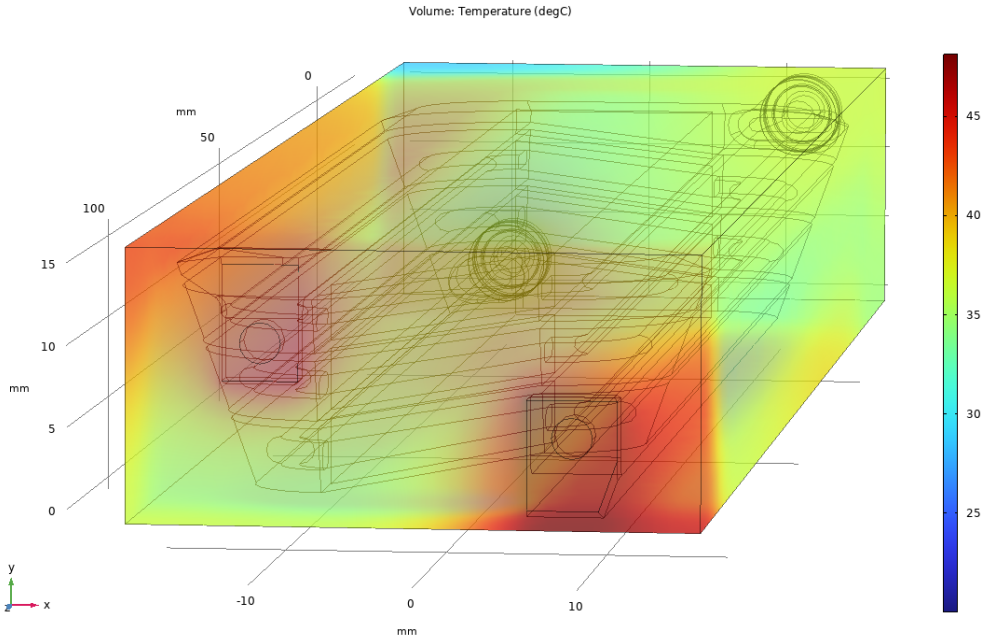

Figure 5.16: Temperature of the winding, cooling fluid, and resin after HT with HFR.

In Fig. 5.17, the temperature of the winding and the cooling fluid is shown. It can be observed that, unlike the previous case, the maximum temperature has decreased to around 47°C.

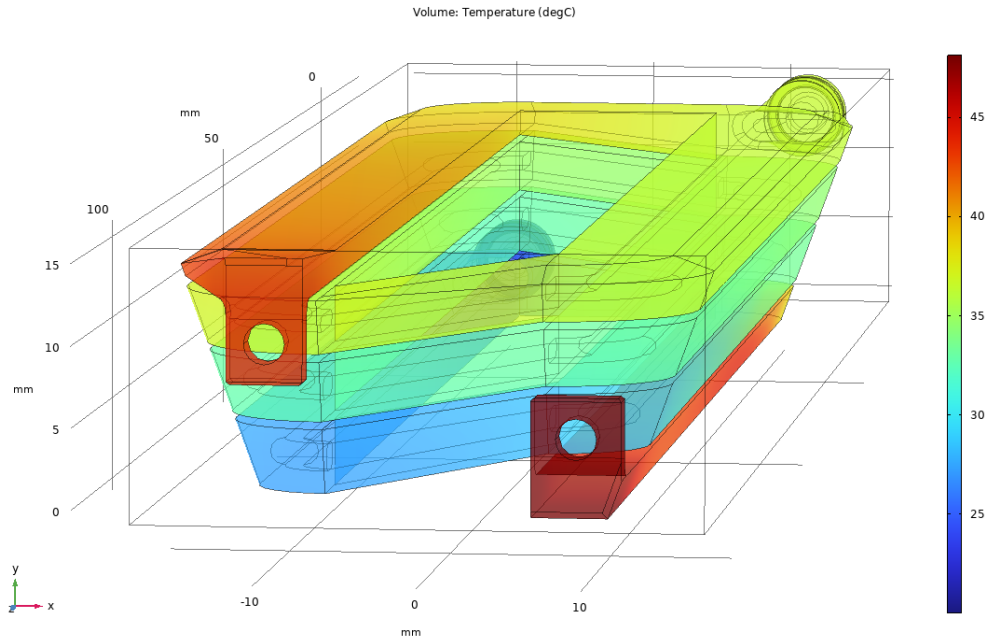

Figure 5.17: Temperature of the winding and cooling fluid after HT with HFR.

In Fig. 5.18, the current density distribution can be seen, and since no parameters other than the cooling fluid flow rate were changed, as expected, it has remained unchanged compared to the previous case.

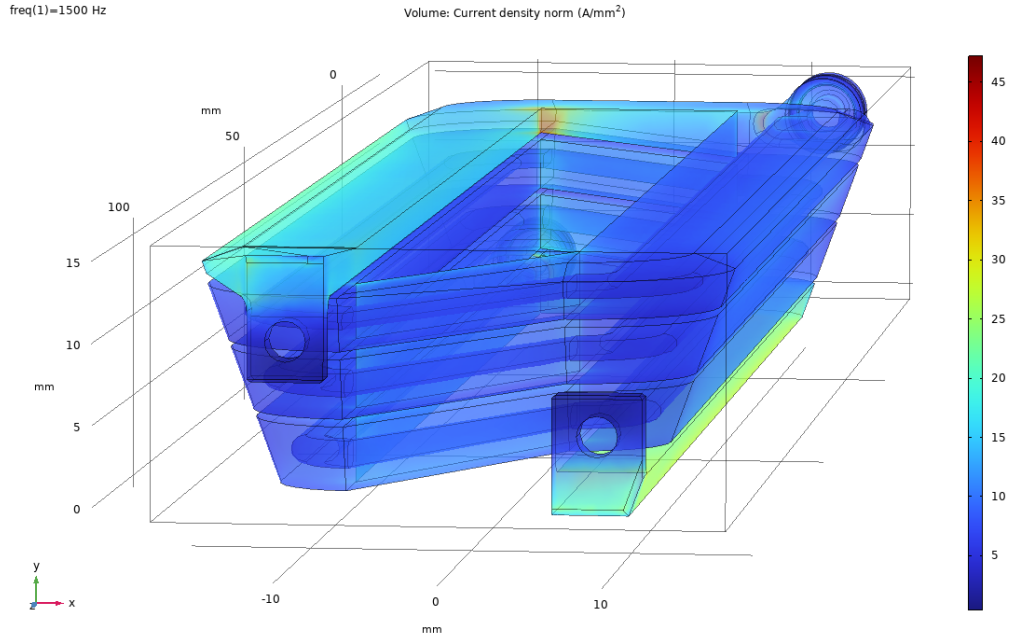

Figure 5.18: Current density after HT with HFR.

Finally, in Fig. 5.19 and Fig. 5.20, it can be observed that the increase in flow rate has led to an increase in fluid velocity within the winding's internal channels, reaching a maximum velocity of about 0.9 m/s. More importantly, it has resulted in a doubling of the pressure difference inside the channels. In fact, by increasing the flow rate from 0.0014 kg/s to 0.0020 kg/s, the pressure variation goes from approximately 330 $mbar$ to around 600 $mbar$.

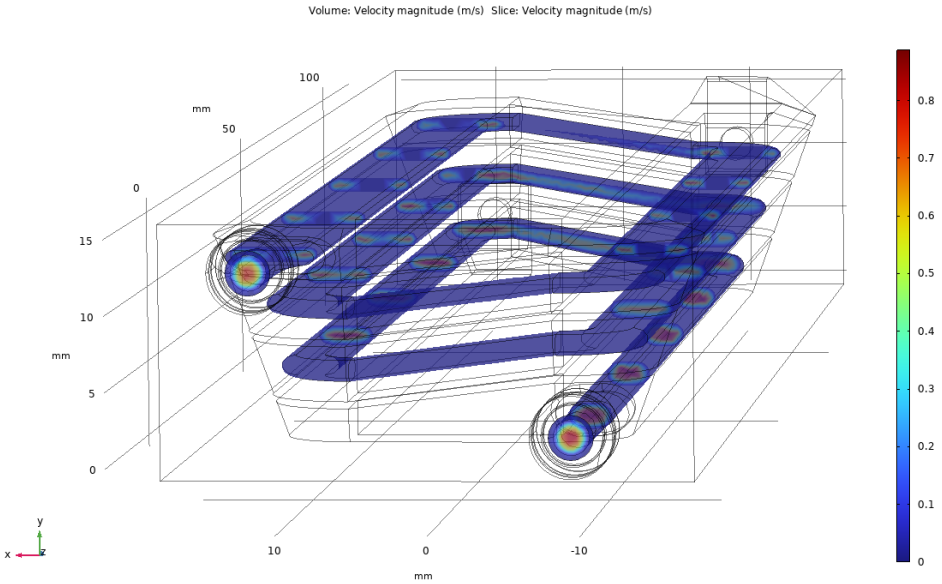

Figure 5.19: Cooling fluid velocity after HT with HFR.

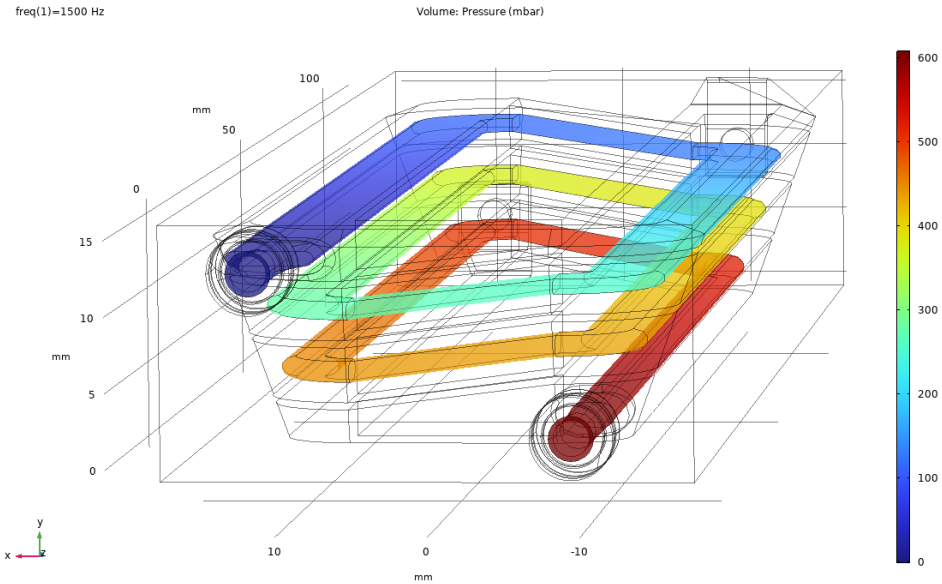

Figure 5.20: Pressure trend after HT with HFR.

Chapter 6

Measurements and comparisons on the printed prototype

In the following chapter, electrical resistance measurements are conducted on the 3D-printed AlSi10Mg prototype. Specifically, the resistance measurement is performed with the winding in the as-built condition, that is, just out of the 3D printer, and after a stress-relieving treatment, in order to observe the differences in the properties of the winding in the two states and to compare the results with those obtained through COMSOL.

6.1 Winding resistance measurement

The winding described in Paragraph 4.3, which had just come out of 3D printing, without any treatment yet (as-built), stripped of its supports, and polished, was subjected to an electrical resistance measurement. Specifically, the resistance measurement was done indirectly, as a DC voltage measurement was taken, and from this, the resistance was calculated.

In detail, the following equipment was used for the measurement:

- For power supply, an *EA ELEKTRO-AUTOMATIK EA-PS 2084-05B* bench power supply set to a constant current of 5.0 A;
- A *Fluke 87V Industrial Multimeter* to ensure the current reaching the winding;
- An *HP Agilent 34401A* for the voltage measurement.

As a first step, the turns of the winding were insulated from each other using sheets of paper, which were more than sufficient for the voltages involved. Then, the current supply terminals were placed on the two electrical terminals of the winding. More precisely, the positive terminal of the power supply was connected directly to the upper terminal of the winding, and the negative terminal was connected to the multimeter, which was then connected to the lower terminal of the winding. A constant DC current of 5.0 A was set on the power supply, and the voltage measurement was performed using probes connected to the *HP Agilent 34401A*, placing the two probes at the two electrical ends of the winding. The measurement returned a value of 19.19 mV. It is specified that the measurements were conducted at 24°C.

In Fig. 6.1, the configuration used for the measurement can be seen.

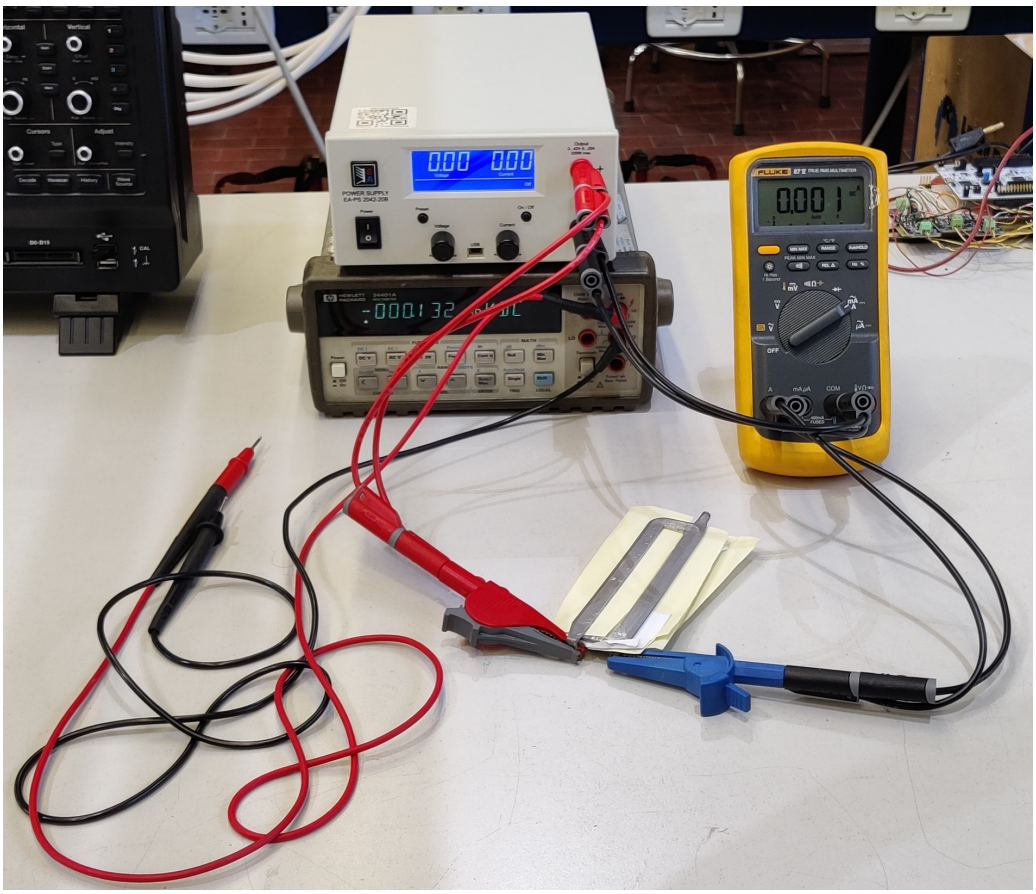

Figure 6.1: Configuration for winding resistance measurement.

With the voltage across the two terminals of the winding and the current flowing through the winding, it is possible to use Ohm's law to calculate the

resistance of the winding:

$$V = R \cdot I \tag{6.1}$$

From which the resistance is obtained:

$$R = \frac{V}{I} = \frac{19.19\,\mathrm{mV}}{5.00\,\mathrm{A}} = 3.838\,\mathrm{m\Omega} \tag{6.2}$$

This value is very similar to the one extrapolated from the COMSOL simulation and to the theoretical value calculated using a spreadsheet, considering the various average cross-sections of the winding coils and the resistivity of AlSi10Mg in *as-built* condition taken from the EOS manual, which corresponds to $\rho = 6.896 \cdot 10^{-8}\,\mathrm{m\Omega}$ and thus to an electrical conductivity of c = $1.450 \cdot 10^{7}\ S/m$, which corresponds to c = 25 %IACS.

In Tab. 6.1, the various results for the resistance of the untreated winding are reported:

Electrical Resistance	**Value**	**Unit**
From measurement	3.838	mΩ
From COMSOL	3.740	mΩ
From spreadsheet	3.914	mΩ

Table 6.1: Resistance values of the as-built winding.

6.2 Measurement after stress-relieving

In this paragraph, the measurement of the winding resistance is carried out after it has undergone stress-relieving. Specifically, stress-relieving is a heat treatment in which the part, after being printed using PBF-LB/M, is heated to a temperature of 270°C for two hours and then cooled in a furnace [25]. The main effects of this treatment are:

- reduction of residual stresses;
- increase in electrical conductivity [22];
- increase in thermal conductivity.

This treatment was performed to improve these properties, as an increase in electrical conductivity leads to lower Joule losses during the winding's operation, and the increase in thermal conductivity allows for more efficient heat exchange, preventing the winding from reaching excessive temperatures.

Having achieved an increase in electrical conductivity, which corresponds to the inverse of electrical resistivity that is proportional to resistance, it is expected that the resistance of the winding has decreased compared to the previous case (as-built). To verify this and to obtain the value of the winding resistance after stress-relieving, two measurements were taken:

- the first in exactly the same manner as described in Paragraph 6.1;
- the second was performed with a micro-ohmmeter.

6.2.1 First measurement configuration

The measurement was conducted exactly in the same manner described in Paragraph 6.1, meaning that a direct current of 5.0 A was passed through the winding, and the voltage across the winding was measured. From this, the resistance was derived using Ohm's law, which is found to be:

$$R = \frac{V}{I} = \frac{10.93\,\mathrm{mV}}{5.00\,\mathrm{A}} = 2.186\,\mathrm{m\Omega} \tag{6.3}$$

From the resistance value, an estimate of the electrical resistivity of the material can be obtained by considering the total length of the winding and taking into account an average cross-section, using the following formula:

$$\rho = \frac{R \cdot S}{L} = \frac{2.186 \cdot 10^{-3}\Omega \cdot 20 \cdot 10^{-6} m^2}{1040 \cdot 10^{-3}} = 4.2038 \cdot 10^{-8}\,\mathrm{m}\Omega \tag{6.4}$$

From which we can calculate the electrical conductivity as follows:

$$c = \frac{1}{\rho} = 2.3788 \cdot 10^{7}\ S/m \tag{6.5}$$

To express the value in %IACS:

$$c_{IACS} = \frac{c}{c_{copper}} \cdot 100 = 41.01\ \%IACS \tag{6.6}$$

In Fig. 6.2, there is a photo of the measurement configuration used.

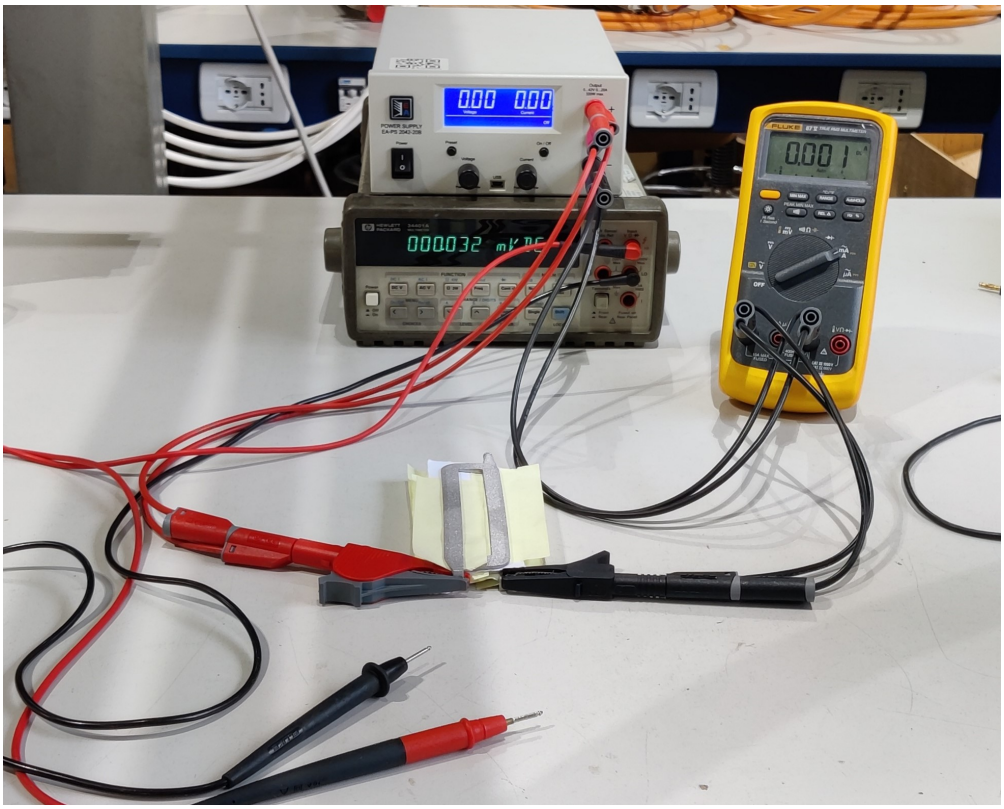

Figure 6.2: Configuration for winding resistance measurement after stress-relieving.

6.2.2 Measurement with micro-ohmmeter

To obtain a more accurate measurement, with a sensitivity in tenths of microohms, a micro-ohmmeter was used, specifically the *DIGITAL MICRO-OHMMETER 32000 points autorange 100 nΩ ÷ 320 Ω model 20022*. In Fig. 6.3, there is a photo of the resistance measurement, with the value still displayed. In particular, it is noted that the resistance value is 2206.6 $\mu\Omega$, which corresponds to 2.2066 $m\Omega$.

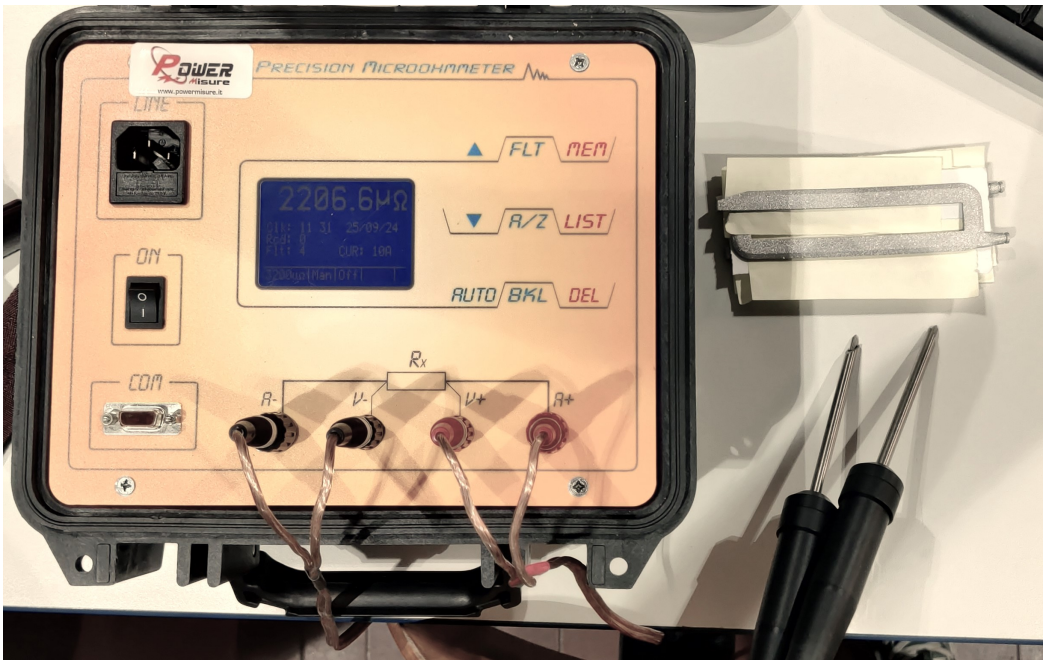

Figure 6.3: Measurement of resistance with a micro-ohmmeter.

As done previously, it is possible to calculate the resistivity and electrical conductivity of the material:

$$\rho = \frac{R \cdot S}{L} = \frac{2.2066 \cdot 10^{-3}\Omega \cdot 20 \cdot 10^{-6} m^2}{1040 \cdot 10^{-3}} = 4.243 \cdot 10^{-8}\,\mathrm{m}\Omega \tag{6.7}$$

$$c = \frac{1}{\rho} = 2.3566 \cdot 10^{7}\, S/m \tag{6.8}$$

To express the value in %IACS:

$$c_{IACS} = \frac{c}{c_{copper}} \cdot 100 = 40.63\ \%IACS \tag{6.9}$$

These resistance values are very similar to those obtained from COMSOL

and from the spreadsheet, where the resistance of the winding was calculated section by section. The resistance values obtained are reported in Tab. 6.2.

Electrical Resistance	**Value**	**Unit**
From first measurement	2.186	mΩ
From micro-ohmmeter	2.2066	mΩ
From COMSOL	2.2798	mΩ
From spreadsheet	2.386	mΩ

Table 6.2: Resistance values of the winding after stress-relieving.

From the values obtained, it can be observed how, thanks to stress-relieving, the resistance of the winding has decreased from approximately 3.8 mΩ to 2.2 mΩ, and how the electrical conductivity has increased from 25 %IACS to around 41 %IACS.

Below, in Fig. 6.4, for completeness, the photos of the winding after stress relieving are shown.

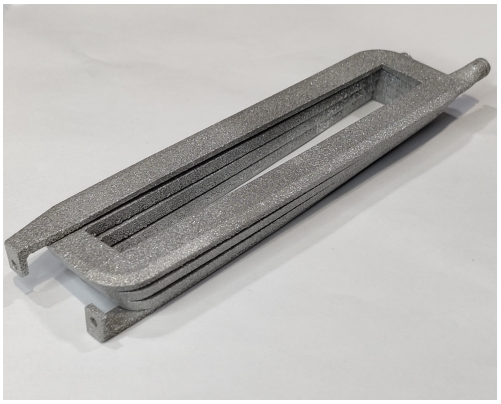

(a) Isometric view of the electrical side

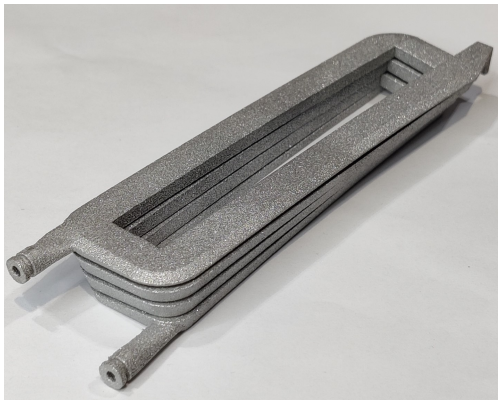

(b) Isometric view of the hydraulic side

(c) Top view.

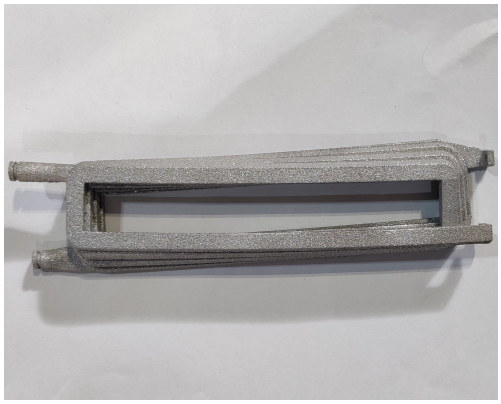

(d) Bottom view.

Figure 6.4: Views of the winding after stress-relieving and shot peening.

Conclusions

This thesis explored the development and analysis of a 3D-printed winding with integrated cooling channels for a multi-three-phase surface permanent magnet motor. The main objective was to reduce the motor's supply voltage from 400 V to 20 V while maintaining a power output of 20 kW, addressing the increased Joule losses with an innovative cooling solution. To achieve this result, the winding was manufactured using Powder Bed Fusion with Laser Beam (PBF-LB/M) technology with the AlSi10Mg alloy, chosen for its optimal mechanical and electrical properties.

Multiphysics simulations conducted with COMSOL allowed for the evaluation of the electrical, thermal, and fluid dynamic performance of the winding, highlighting how the integration of cooling channels effectively reduces the system's operating temperature. The simulation results were then compared with experimental measurements performed on the printed prototype, showing a good correlation between the simulated and real data.

The results demonstrate that additive manufacturing, combined with advanced multiphysics analysis, represents a powerful and innovative approach for optimizing the design of complex electrical components. This methodology not only improves thermal management but also enables the creation of complex geometries and cooling solutions that would be impossible to achieve with traditional manufacturing methods.

Future prospects include exploring other materials with improved properties, further optimizations of the cooling channel design, and applying this approach to other types of electric motors. Additionally, further refinement of the printing parameters could reduce production defects and further enhance the mechanical and electrical performance of the printed components.

Bibliography

[1] Amir Mostafaei, Cang Zhao, Yining He, Seyed Reza Ghiaasiaan, Bo Shi, Shuai Shao, Nima Shamsaei, Ziheng Wu, Nadia Kouraytem, Tao Sun, Joseph Pauza, Jerard V. Gordon, Bryan Webler, Niranjan D. Parab, Mohammadreza Asherloo, Qilin Guo, Lianyi Chen, and Anthony D. Rollett. Defects and anomalies in powder bed fusion metal additive manufacturing. *Current Opinion in Solid State and Materials Science*, 26(2):100974, 2022. ISSN 1359-0286. doi: https://doi.org/10.1016/j.cossms.2021.100974. URL `https://www.sciencedirect.com/science/article/pii/S1359028621000772`.

[2] F. Calignano. Design optimization of supports for overhanging structures in aluminum and titanium alloys by selective laser melting. *Materials Design*, 64:203–213, 2014. ISSN 0261-3069. doi: https://doi.org/10.1016/j.matdes.2014.07.043. URL `https://www.sciencedirect.com/science/article/pii/S0261306914005755`.

[3] Michela Diana. *Tooth-coil wound multiphase synchronous machines*. PhD thesis, Politecnico di Torino, 2018. Doctoral Dissertation.

[4] EOS GmbH Electro Optical Systems. *EOS Aluminium AlSi10Mg Material Data Sheet*. EOS GmbH Electro Optical Systems, Robert-Stirling-Ring 1, D-82152 Krailling/Munich, Germany, January 2022. URL `https://www.eos.info/03_system-related-assets/material-related-contents/metal-materials-and-examples/metal-material-datasheet/aluminium/material_datasheet_eos_aluminium-alsi10mg_en_web.pdf`. Status 01/2022.

[5] Diego Manfredi, Flaviana Calignano, Manickavasagam Krishnan, Riccardo Canali, Elisa Paola Ambrosio, Sara Biamino, Daniele Ugues, Matteo Pavese, and Paolo Fino. Additive manufacturing of al alloys and

aluminium matrix composites (amcs). In Waldemar A. Monteiro, editor, *Light Metal Alloys Applications*, chapter 1. IntechOpen, Rijeka, 2014. doi: 10.5772/58534. URL https://doi.org/10.5772/58534.

[6] Leticia Cabrera-Correa, Leandro González-Rovira, Juan de Dios López-Castro, and F. Javier Botana. Pitting and intergranular corrosion of scalmalloy® aluminium alloy additively manufactured by selective laser melting (slm). *Corrosion Science*, 201:110273, 2022. ISSN 0010-938X. doi: https://doi.org/10.1016/j.corsci.2022.110273. URL https://www.sciencedirect.com/science/article/pii/S0010938X22001913.

[7] V.A. Medrano, E. Arrieta, J. Merino, B. Ruvalcaba, K. Caballero, B. Ramirez, J. Diemann, L.E. Murr, R.B. Wicker, D. Godfrey, M. Benedict, and F. Medina. A comprehensive and comparative study of microstructure and mechanical properties for post-process heat treatment of alsi7mg alloy components fabricated in different laser powder bed fusion systems. *Journal of Materials Research and Technology*, 24:6820–6842, 2023. ISSN 2238-7854. doi: https://doi.org/10.1016/j.jmrt.2023.04.129. URL https://www.sciencedirect.com/science/article/pii/S2238785423008220.

[8] Woo Jin Hwang, Gyung Bae Bang, and Sung-Hoon Choa. Effect of a stress relief heat treatment of AlSi7Mg and AlSi10Mg alloys on mechanical and electrical properties according to silicon precipitation. *Metals and Materials International*, 29(5):1311–1322, May 2023. ISSN 2005-4149. doi: 10.1007/s12540-022-01304-7. URL https://doi.org/10.1007/s12540-022-01304-7.

[9] Hao Wang, Liang Guo, Zhen Nie, Qitao Lyu, and Qingmao Zhang. Processing technologies and properties of cu-10sn formed by selective laser melting combined with heat treatment. *3D Printing and Additive Manufacturing*, 8(1):13–22, 2021. doi: 10.1089/3dp.2020.0192. URL https://doi.org/10.1089/3dp.2020.0192.

[10] SLM Solutions Group AG. Material data sheet cu-alloy cuni2sicr, 2019. URL https://www.slm-solutions.com/fileadmin/Content/Powder/MDS/MDS_Cu-Alloy_CuNi2SiCr_0919_EN.pdf. Accessed: 2024-07-20.

[11] ELANTAS Italia S.r.l. *Elan-tron MC 62/W 363*. ELANTAS Italia S.r.l., Strada Antolini n° 1, 43044 Collecchio (PR), Italy, December 2012. URL `https://www.elantas.com`. Rev. n. 12.

[12] Anton Wiberg, Johan Persson, and Johan Ölvander. Design for additive manufacturing – a review of available design methods and software. *Rapid Prototyping Journal*, 25(6):1080–1094, Jul 2019. doi: 10.1108/rpj-10-2018-0262.

[13] ASTM International. Additive manufacturing — general principles — fundamentals and vocabulary, 2021. URL `https://www.iso.org/obp/ui/#iso:std:iso-astm:52900:ed-2:v1:en`. ISO/ASTM52900.

[14] Flaviana Calignano, Diego Manfredi, Elisa Paola Ambrosio, Sara Biamino, Mariangela Lombardi, Eleonora Atzeni, Alessandro Salmi, Paolo Minetola, Luca Iuliano, and Paolo Fino. Overview on additive manufacturing technologies. *Proceedings of the IEEE*, 105(4):593–612, 2017. doi: 10.1109/JPROC.2016.2625098.

[15] Nesma T. Aboulkhair, Nicola M. Everitt, Ian Ashcroft, and Chris Tuck. Reducing porosity in alsi10mg parts processed by selective laser melting. *Additive Manufacturing*, 1-4:77–86, 2014. ISSN 2214-8604. doi: https://doi.org/10.1016/j.addma.2014.08.001. URL `https://www.sciencedirect.com/science/article/pii/S2214860414000062`. Inaugural Issue.

[16] Ruidi Li, Jinhui Liu, Yusheng Shi, Li Wang, and Wei Jiang. Balling behavior of stainless steel and nickel powder during selective laser melting process. *The International Journal of Advanced Manufacturing Technology*, 59(9–12):1025–1035, Aug 2011. doi: 10.1007/s00170-011-3566-1.

[17] A. Mansoura, N. Omidi, N. Barka, S. S. Kangranroudi, and S. Dehghan. Selective laser melting of stainless steels: A review of process, microstructure and properties. *Metals and Materials International*, 2024. doi: 10.1007/s12540-024-01650-8.

[18] Cassidy Silbernagel, Ian Ashcroft, Phill Dickens, and Michael Galea. Electrical resistivity of additively manufactured alsi10mg for use in electric motors. *Additive Manufacturing*, 21:395–403, 2018. ISSN 2214-8604.

doi: https://doi.org/10.1016/j.addma.2018.03.027. URL https://www.sciencedirect.com/science/article/pii/S2214860418300769.

[19] Leticia Cabrera-Correa, Leandro González-Rovira, Juan de Dios López-Castro, Miguel Castillo-Rodríguez, and F. Javier Botana. Effect of the heat treatment on the mechanical properties and microstructure of scalmalloy® manufactured by selective laser melting (slm) under certified conditions. *Materials Characterization*, 196:112549, 2023. ISSN 1044-5803. doi: https://doi.org/10.1016/j.matchar.2022.112549. URL https://www.sciencedirect.com/science/article/pii/S1044580322008312.

[20] Min Wang, Jianbao Gao, Lijun Zhang, and Bo Song. A new alsi7mg-xsc alloy with high strength and high strain manufactured by selective laser melting. *Journal of Materials Research and Technology*, 30:4272–4282, 2024. ISSN 2238-7854. doi: https://doi.org/10.1016/j.jmrt.2024.04.123. URL https://www.sciencedirect.com/science/article/pii/S2238785424008974.

[21] Shuai Huang, Shao-qing Guo, Biao Zhou, Guo-hui Zhang, and Xue-jun Zhang. Microstructure and properties of alsi7mg alloy fabricated by selective laser melting. *China Foundry*, 18(4):416–423, July 2021. ISSN 2365-9459. doi: 10.1007/s41230-021-1004-z. URL https://doi.org/10.1007/s41230-021-1004-z.

[22] Silvia Marola, Oscar Antonio Peverini, Mauro Lumia, Giuseppe Addamo, Flaviana Calignano, and Diego Manfredi. Effect of thermal treatments on the surface electrical conductivity of alsi7mg produced by laser powder bed fusion. *Materials Today Communications*, 39:109339, 2024. ISSN 2352-4928. doi: https://doi.org/10.1016/j.mtcomm.2024.109339. URL https://www.sciencedirect.com/science/article/pii/S2352492824013205.

[23] Congyuan Zeng, Bin Zhang, Ali Hemmasian Ettefagh, Hao Wen, Hong Yao, W.J. Meng, and Shengmin Guo. Mechanical, thermal, and corrosion properties of cu-10sn alloy prepared by laser-powder-bed-fusion additive manufacturing. *Additive Manufacturing*, 35:101411, 2020. ISSN 2214-

8604. doi: https://doi.org/10.1016/j.addma.2020.101411. URL https://www.sciencedirect.com/science/article/pii/S2214860420307831.

[24] Ayman M. EL-Refaie. Fractional-slot concentrated-windings synchronous permanent magnet machines: Opportunities and challenges. *IEEE Transactions on Industrial Electronics*, 57(1):107–121, 2010. doi: 10.1109/TIE.2009.2030211.

[25] P. Van Cauwenbergh, V. Samaee, L. Thijs, J. Nejezchlebová, P. Sedlák, A. Iveković, D. Schryvers, B. Van Hooreweder, and K. Vanmeensel. Unravelling the multi-scale structure-property relationship of laser powder bed fusion processed and heat-treated alsi10mg. *Scientific Reports*, 11: 6423, 2021. doi: 10.1038/s41598-021-85047-2.